

# Specific heat and gap structure of a nematic superconductor: Application to FeSe

Kazi Ranjibul Islam,<sup>1,\*</sup> Jakob Böker,<sup>2,\*</sup> Ilya M. Eremin,<sup>2</sup> and Andrey V. Chubukov<sup>1</sup>

<sup>1</sup>*School of Physics and Astronomy and William I. Fine Theoretical Physics Institute,  
University of Minnesota, Minneapolis, Minnesota 55455, USA*

<sup>2</sup>*Institut für Theoretische Physik III, Ruhr-Universität Bochum, 44801 Bochum, Germany*



(Received 24 June 2021; revised 8 September 2021; accepted 10 September 2021; published 27 September 2021)

We report the results of our in-depth analysis of spectroscopic and thermodynamic properties of a multiorbital metal, like FeSe, which first develops a nematic order and then undergoes a transition into a superconducting state, which coexists with nematicity. We analyze the angular dependence of the gap function and specific heat  $C_v(T)$  of such a nematic superconductor. We specifically address three issues: (i) the angular dependence of the gap in light of the competition between the nematicity-induced  $s$ - $d$  mixture and the orbital transmutation of low-energy excitations in the nematic state, (ii) the effect of nematicity on the magnitude of the jump of the specific heat  $C_v(T)$  at  $T_c$  and the temperature dependence of  $C_v(T)$  below  $T_c$ , and (iii) a potential transition at  $T_{c1} < T_c$  from an  $s + d$  state to an  $s + e^{in}d$  state that breaks time-reversal symmetry. We consider two scenarios for a nematic order: scenario A, in which this order develops between  $d_{xz}$  and  $d_{yz}$  orbitals on hole and electron pockets, and scenario B, in which there is an additional component of the nematic order for  $d_{xy}$  fermions on the two electron pockets.

DOI: [10.1103/PhysRevB.104.094522](https://doi.org/10.1103/PhysRevB.104.094522)

## I. INTRODUCTION

Iron-based unconventional superconductors demonstrate remarkable properties, which include multiorbital low-energy electronic states and ubiquity of the nematic phase. A particularly interesting situation occurs when superconductivity is preceded by the development of a nematic order that breaks  $C_4$  lattice rotational symmetry down to  $C_2$ . The most prominent example of this so-called nematic superconductor is FeSe, in which a nematic order develops at  $T_n \sim 90$  K at ambient pressure, while superconductivity develops at a much lower  $T_c \sim 9$  K, out of a nematic state [1,2]. Nematic superconductivity has been observed also in other Fe-based materials, but there the difference between  $T_n$  and  $T_c$  is much smaller [3]. It has also been argued that in some cases a nematic order does not exist in the normal state but is induced by superconductivity. A candidate for such behavior in the Fe-family is LiFeAs [4]; the same behavior has been reported in twisted bilayer graphene [5] and in a doped topological insulator  $R_x\text{Bi}_2\text{Se}_3$  ( $R = \text{Cu}, \text{Nb}, \text{and Sr}$ ) [6–9]. In this work, we focus on the theoretical analysis of the spectroscopic and the thermodynamic properties of such a nematic superconductor using the case of FeSe, where  $T_n$  is substantially larger than  $T_c$ . The electronic structure of FeSe in the tetragonal phase consists of two hole pockets, centered around the  $\Gamma$  point (the inner one and the outer one), and electron pockets, centered around the  $X$  and the  $Y$  points of the Brillouin zone, respectively [Fig. 1(a)]. Here, we use the notation of the 1-Fe unit cell. The hole pockets and the corresponding bands are composed of fermions from  $d_{xz}$  and  $d_{yz}$  orbitals, the  $X$ -pocket/band is a mixture of  $d_{yz}$  and  $d_{xy}$

orbitals, and the  $Y$ -pocket/band is a mixture of  $d_{xz}$  and  $d_{xy}$  orbitals. Angle-resolved photoemission spectroscopy (ARPES) studies revealed that in FeSe the inner-hole pocket is quite small in the tetragonal phase and disappears in the presence of a nematic order when the corresponding band sinks below the Fermi level [12] [Fig. 1(b)]. The inner-hole band then does not affect system behavior at low energies, and we neglect it in our analysis. For the outer-hole pocket, the orbital content in the tetragonal phase is predominantly  $d_{xz}$  along the  $k_y$ -direction and  $d_{yz}$  along the  $k_x$ -direction.

We consider two scenarios for the nematic order,  $\Phi$ . In the first (scenario A) we assume that  $\Phi$  splits the occupations of  $d_{xz}$  and  $d_{yz}$  orbitals:

$$\Phi_{xz/yz} = \langle d_{xz}^\dagger d_{xz} - d_{yz}^\dagger d_{yz} \rangle. \quad (1)$$

Furthermore, we follow earlier theoretical and experimental studies [13–17], which showed that such  $\Phi$  changes sign between hole and electron pockets. We label  $\Phi$  on the outer-hole pocket as  $\Phi_h$  and the one on the  $Y$  and the  $X$  electron pockets as  $\Phi_e$  ( $\text{sgn } \Phi_e = -\text{sgn } \Phi_h$ ). In the second scenario (scenario B), we assume that in addition to  $\Phi_{h,e}$ , nematicity gives rise to a substantial difference between occupations of  $d_{xy}$  fermions on the  $Y$  and the  $X$  pockets [11,13,18,19]. The corresponding nematic order parameter is then given by

$$\Phi_{xy} = \langle d_{xy,Y}^\dagger d_{xy,Y} - d_{xy,X}^\dagger d_{xy,X} \rangle. \quad (2)$$

Scenario B was recently advanced in Ref. [11] as a way to explain the thermal evolution of the band structure across the tetragonal to orthorhombic transition as well as the fact that ARPES and quasiparticle interference (QPI) measurements in the nematic phase detect a peanut-shaped  $X$  pocket, but do not see the  $Y$  pocket [20–25]. The argument here is that for large enough  $\Phi_{xy}$ , the  $Y$  pocket disappears, as its bottom moves above the Fermi level [Fig. 1(d)]. A similar behavior has been

\*These authors contributed equally to this work.

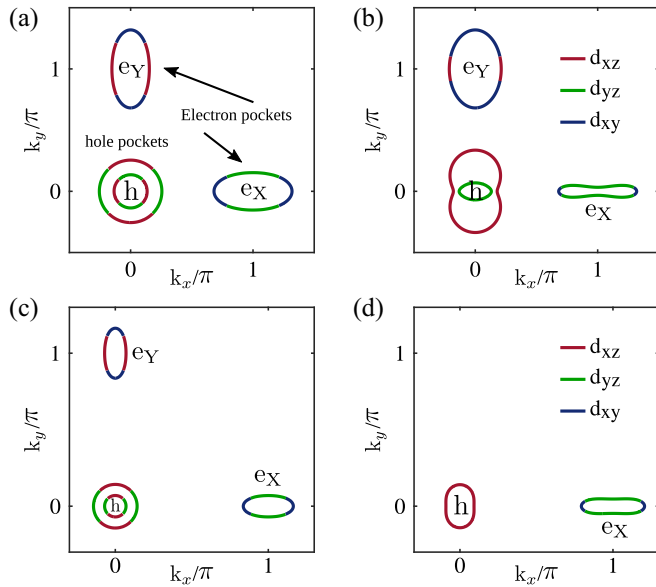


FIG. 1. Fermi surface topology in 1-Fe unit cell of FeSe in the tetragonal phase (a), (c) and the orthorhombic (nematic) phase (b), (d). The Fermi surface evolution in (b) results from sign-changing nematic order involving  $d_{xz}$  and  $d_{yz}$  orbitals; in (d) it additionally involves sizable nonlocal  $d_{xy}$  nematic order. We refer to panels (b) and (d) as “scenario A” and “scenario B,” respectively. The color code follows the major orbital content. Fitting parameters for (a), (b) are taken from Refs. [3,10], and those for (c), (d) are from Ref. [11].

obtained in monoclinic systems by allowing a nonzero interorbital  $d_{xz}$ - $d_{xy}$  and  $d_{yz}$ - $d_{xy}$  nematicity [26]. Within scenario A, it was argued [27] that the  $Y$  pocket is not observed, because in the nematic phase it becomes predominantly  $d_{xy}$  [the blue ellipse in Fig. 1(b)], and these excitations are less coherent than the ones for  $d_{xz}$  and  $d_{yz}$  fermions [28]. In this work, we analyze the effect of nematicity on the superconducting state within both scenarios. We discuss the angular dependence of the superconducting gap, most notably on the hole pockets, and the behavior on the specific heat  $C(T)$  at and below  $T_c$ .

Multiorbital superconductivity in Fe-based materials in the absence of a nematic order has been extensively studied by many groups [2,29–33]. A mixed orbital content of low-energy excitations implies that the pairing interaction necessarily has two orthogonal components:  $s$ -wave and  $d$ -wave, even when the interaction is local in the orbital basis. An  $s$ -wave interaction is attractive in the  $s^{+-}$  subchannel (the sign of the gap on the hole pocket is opposite to that on electron  $X$  and  $Y$  pockets), a  $d$ -wave interaction is attractive in the  $d_{x^2-y^2}$  subchannel (the gap on the hole pocket scales as  $\cos 2\theta$ , where  $\theta$  is the angle along the pocket, and it has four nodes, while the gaps on the  $X$  and the  $Y$  pocket have opposite sign). In both cases, the gaps on the  $X$  and  $Y$  pockets are sign-preserving, but generally have minima at the points where  $d_{xz}$  ( $d_{yz}$ ) orbital content vanishes. These minima can become nodes if  $d_{xy}$  orbitals contribute to superconductivity [11].

The pairing interaction in the  $s$ -wave and the  $d$ -wave channels is expressed in terms of dressed interactions between hole and electron pockets: intraorbital density-density interaction  $U_{he}$ , and interorbital pair-hopping interactions  $J_{he}$  and

$J_{ee}$  (see Sec. III below). The terms  $U_{he}$  and  $J_{he}$  are enhanced by magnetic fluctuations with momenta near  $(0, \pi)$  and  $(\pi, 0)$  (the distances between the centers of the  $\Gamma$  and the  $X$  and the  $Y$  pockets, respectively), and  $J_{ee}$  is enhanced by magnetic fluctuations with momentum  $(\pi, \pi)$  (the distance between the  $X$  and the  $Y$  pockets). We follow earlier works [34,35] and assume that the dressed pairing interaction in the tetragonal phase is somewhat stronger in the  $s^{+-}$  channel. This implies that the pairing state without nematic order would be  $s^{+-}$ .

Superconductivity in the presence of a small nematic order  $\Phi_{h,e}$  has been studied previously in Refs. [34–36]. The expected outcome is that a nematic order mixes  $s$ -wave and  $d$ -wave pairing channels, creating a mixed  $s + d$  state. A general belief, coming from small  $\Phi_{h,e}$  analysis, is that in such a state the gap along the hole pocket is  $\Delta_h(\theta) = \Delta_s + \Delta_d \cos 2\theta$ , where  $\theta$  is the angle along the pocket. The magnitude of  $\Delta_d$  increases with  $\Phi$ , and if one would extend the small  $\Phi$  analysis to larger  $\Phi$ , one would obtain that  $\Delta_h(\theta)$  develops a deep minima and then accidental nodes. This reasoning has been applied to explain ARPES and scanning tunneling microscopy (STM) data in FeSe [20,36,37]. We argue that this is not necessarily the case because there is a second, competing effect of nematicity. Namely, a nematic order changes the orbital composition of the pockets (this phenomenon has been termed orbital transmutation [17]). This leads to two effects. First, the variable  $\theta$  gets renormalized and becomes dependent on  $\Phi_h$ . At large enough  $\Phi_h$ , the dressed  $\theta$  (called  $\phi$  later in the paper) clusters near  $\pm\pi/2$ , depending on the sign of  $\Phi_h$ , and the gap loses its angle dependence. Second, the ratio  $\Delta_d/\Delta_s$  becomes a nonlinear function of  $\Phi_h$ , and the ratio  $\Phi_h/\Phi_e$ . Furthermore, in some intervals of  $\Phi_h/\Phi_e$  it remains below 1 even at large  $\Phi_h$  values. This prevents the appearance of the nodes even if the angular variation of the  $d$ -wave gap component is still a sizable one.

Our goal is to understand what happens at intermediate values of  $\Phi$ , relevant to FeSe, particularly whether there exists the range of  $\Phi_h$  and  $\Phi_h/\Phi_e$ , where  $\Delta_h$  has nodes. We show that this range exists, but is confined to near-equal interactions in  $s$ -wave and  $d$ -wave channels. Nevertheless, even if the gap does not have nodes, its angular variation follows the orbital content of the hole pocket and undergoes a strong evolution once the orbital content changes. For completeness, we also consider the case when the  $d$ -wave interaction is stronger than the one in the  $s^{+-}$  channel. In this case, the gap has four nodes at small  $\Phi_{h,e}$  and no nodes at large  $\Phi_{h,e}$ , due to orbital transmutation. We show that the transformation of the nodal structure at intermediate  $\Phi_{h,e}$  is rather involved, and for some  $\Phi_e/\Phi_h$  there exists an intermediate gap configuration with eight nodes.

We next consider the behavior of the specific heat  $C_v(T)$  at and below  $T_c$ . We analyze how the jump of  $C_v(T)$  varies with the type of nematic order and whether the jump primarily comes from fermions from  $d_{xz}$  and  $d_{yz}$  orbitals, or if there is a sizable contribution from the  $d_{xy}$  orbital. A similar issue has been recently studied [38] for  $\text{KFe}_2\text{As}_2$ . There, the  $d_{xy}$  orbital gives the dominant contribution to  $C_v(T)$  in the normal state because of the large mass of  $d_{xy}$  fermions, but contributes little to the jump of  $C_v(T)$  and also to the temperature dependence of  $C_v(T)$  in a wide temperature region below  $T_c$ , because a superconducting gap on this orbital is inversely proportional

to its mass and is much smaller than the ones on  $d_{xz}$  and  $d_{yz}$  orbitals. We analyze whether the same holds for FeSe, using the values of quasiparticle masses, extracted from ARPES. We find that the jump of the specific heat at  $T_c$  is smaller than in BCS theory for the same number of pockets. For the same reason as in  $\text{KFe}_2\text{As}_2$ ,  $d_{xy}$  fermions substantially contribute to  $C_v(T)$  in the normal state but little to the jump of  $C_v(T)$  at  $T_c$ . We decompose  $\Delta C_v$  into contributions from different pockets and show that the largest contribution comes from fermions on a hole pocket in scenario A and from an electron pocket in scenario B. We analyze how  $\Delta C_v$  evolves with nematic order and again find a strong correlation with the orbital transmutation.

Finally, we address the issue of a potential second transition to the new phase within the superconducting state. The argument here is that in a situation when the attraction in the  $d_{x^2-y^2}$  channel is comparable to that in the  $s^{+-}$  channel, a biquadratic coupling between  $s$ - and  $d$ -order parameters may turn the  $s + d$  pairing state into an  $s + ie^{in}d$  state (the analog of a mixed  $s + id$  state in the absence of nematicity). Such a state breaks  $Z_2$  time-reversal symmetry, as the relative factor can be either  $i$  or  $-i$ . Recent specific-heat measurements,  $C_v(T)$ , of FeSe [39–44] found an anomaly at  $T \sim 1$  K, which might indicate the emergence of  $s + e^{in}d$  order [35]. To verify the scenario, we vary the relative strength of the pairing interactions in  $s$ -wave and  $d$ -wave channels, and we analyze the Landau functional including both the bi-quadratic couplings between  $s$ - and  $d$ -gap components and the effect of orbital transmutation in the nematic phase. Although the orbital transmutation shrinks the parameter range of the  $s + e^{in}d$  state, a transition into an  $s + e^{in}d$  state below  $T_c$  is still possible.

The structure of the paper is the following. In the next section, we briefly discuss the electronic structure of FeSe. In Sec. III A, we obtain the pairing interaction within scenario A, convert it into the band basis, and solve for the pairing gaps on hole and electron pockets. In Sec. III B we analyze the angular dependence of the gap on the hole pocket at various  $\Phi_h$  and  $\Phi_h/\Phi_e$ . In Sec. III C we study the temperature dependence of the gap below  $T_c$ . In Sec. IV we compute the jump of the specific heat at  $T_c$  within both scenarios and compare them to the available experimental data. We decompose the jump into contributions from different orbitals and study their relative strength. We also compute specific heat at  $T < T_c$ . In Sec. V we consider a putative transition into the  $s + e^{in}d$  state. Finally, we present our conclusions in Sec. VI.

## II. THE BAND HAMILTONIAN

As mentioned in the Introduction, we consider a two-dimensional three-band/three-pocket model Hamiltonian with a hole pocket, centered at the  $\Gamma$  point of the BZ, and two electron pockets, centered at  $X = (0, \pi)$  and  $Y = (\pi, 0)$  points of the Brillouin zone, respectively. For simplicity, we neglect the effect of spin-orbit coupling on the band dispersion. The hole pocket and the corresponding hole band are composed of  $d_{xz}$  and  $d_{yz}$  orbitals. The  $X$ -pocket/band is composed of  $d_{yz}$  and  $d_{xy}$  orbitals, and the  $Y$ -pocket/band is composed of  $d_{xz}$  and  $d_{xy}$  orbitals. We introduce two-component spinors  $\psi_\Gamma = (d_{xz}, d_{yz})^T$  and

TABLE I. Band parameters for the hole pocket.

$\mu_h$	$(2m_h)^{-1}$	$b$
13.6	473	529

$\psi_{X/Y} = (d_{yz/xz}, d_{xy})^T$ , and we write the kinetic energy  $H_0$  as

$$H_0 = H_\Gamma + H_X + H_Y, \quad (3)$$

where each term is bilinear in spinors. For scenario A we introduce the nematic order  $\Phi$  as the difference in the occupation of  $d_{xz}$  and  $d_{yz}$  orbitals; see Eq. (1). We define  $\Phi$  on the hole pocket as  $\Phi_h$  and on the electron pocket as  $\Phi_e$ . The latter is the difference in the occupation of the  $d_{xz}$  orbital on the  $Y$  pocket and the  $d_{yz}$  orbital on the  $X$  pocket. For scenario B we additionally introduce a second component of a nematic order as the difference between occupations of  $d_{xy}$  orbitals on the  $Y$  and  $X$  pockets; see Eq. (2).

### A. Hole pocket

The band Hamiltonian for the hole pocket  $H_\Gamma$  is [17,34,45,46]

$$H_\Gamma = \psi_\Gamma^\dagger \left[ \left( \mu_h - \frac{\mathbf{k}^2}{2m_h} \right) \tau_0 - \left( \frac{b}{2} \mathbf{k}^2 \cos 2\theta_h - \Phi_h \right) \tau_3 - c \mathbf{k}^2 \sin 2\theta_h \tau_1 \right] \psi_\Gamma, \quad (4)$$

where  $\theta_h$  is the polar angle for momentum  $\mathbf{k}$ , measured from the  $k_x$ -direction in the anticlockwise direction. We set  $c = -\frac{b}{2}$ , which yields circular hole pockets in the tetragonal phase. The parameters of Eq. (4) are listed in Table I, and they were obtained in Refs. [3,10] from fitting to ARPES data for FeSe at  $k_z = \pi$ . Diagonalizing Eq. (4), we obtain two dispersions. In the absence of nematicity, they give rise to the outer- and the inner-hole pockets, Fig. 3(a). At a finite  $\Phi_h > \mu_h$ , the inner-hole pocket becomes very shallow and then disappears as the corresponding dispersion sinks below the Fermi level. For this reason, we neglect the inner-hole band in our analysis of the low-energy physics.

The larger hole Fermi surface pocket survives at a finite  $\Phi_h$  and becomes elliptical. The dispersion of the corresponding band is

$$\xi_h(\mathbf{k}) = \mu_h - \frac{\mathbf{k}^2}{2m_h} + \sqrt{\Phi_h^2 + b^2 \frac{\mathbf{k}^4}{4} - b \mathbf{k}^2 \Phi_h \cos 2\theta_h}; \quad (5)$$

see Fig. 3(b). The band operator  $h$  is a linear combination of fermionic operators from  $d_{xz}$  and  $d_{yz}$  operators:

$$h = \cos \phi_h d_{yz} + \sin \phi_h d_{xz}, \quad (6)$$

where the momentum label ( $\mathbf{k}$ ) is implicit, and  $\phi_h$  is defined via

$$\cos 2\phi_h = \frac{b \frac{\mathbf{k}^2}{2} \cos 2\theta_h - \Phi_h}{\sqrt{\Phi_h^2 + b^2 \frac{\mathbf{k}^4}{4} - b \mathbf{k}^2 \Phi_h \cos 2\theta_h}}. \quad (7)$$

At  $\Phi_h = 0$ ,  $\phi_h = \theta_h$ , and  $d_{yz}$  and  $d_{xz}$  fermions contribute to  $h$  with weights  $|\langle d_{yz} | h \rangle|^2 = \cos^2 \theta_h$  and  $|\langle d_{xz} | h \rangle|^2 = \sin^2 \theta_h$ , simply related by  $\pi/2$  rotation. At a nonzero  $\Phi_h$ ,  $\phi_h$  becomes different from  $\theta_h$ , and the weight of the two orbitals is no

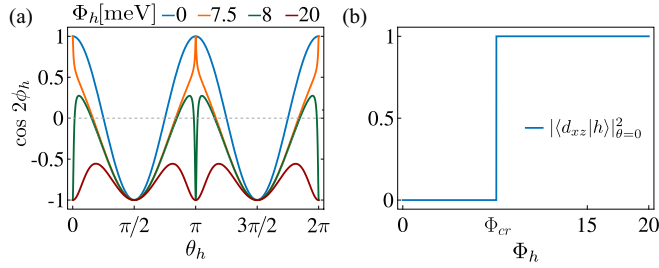


FIG. 2. (a) Angular variation of  $\cos 2\phi_h$  along the hole Fermi pocket for selected values of  $\Phi_h$ , (b) the  $d_{xz}$  orbital weight at  $\theta_h = 0$  as a function of  $\Phi_h$ .

longer equal. At large  $\Phi_h$ ,  $\cos 2\phi_h = -\text{sgn}\Phi_h$ . Choosing for definiteness  $\Phi_h > 0$ , we find that  $\phi_h = \pi/2$ , hence the band operator  $h$  in Eq. (6) becomes entirely  $d_{xz}$ , i.e., the hole pocket becomes mono-orbital. This effect has been dubbed “orbital transmutation” [17,46]. The angular variation of  $\cos 2\phi_h$  on the outer-hole pocket for intermediate values of  $\Phi_h$  is shown in Fig. 2(a). At  $\Phi_h = \Phi_{\text{cr}} = bk_F^2/2 = \mu_h m_h b$ ,  $\cos 2\phi_h$  along the  $k_x$ -direction jumps discontinuously from +1 to -1 [orange and green curves in Fig. 2(a)], and the orbital content jumps from a pure  $d_{yz}$  to a pure  $d_{xz}$  [see Fig. 2(b)]. Because of that jump, the angular average of  $\cos 2\phi_h$  and  $\cos^2 2\phi_h$  along the hole Fermi surface, viewed as a function of  $\Phi_h$ , becomes non-analytic at  $\Phi_{\text{cr}}$ . In addition, at  $\Phi \geq \Phi_{\text{cr}}$ , the number of nodes of  $\cos 2\phi_h$  on the Fermi surface increases from 4 to 8 [the green curve in Fig. 2(a)]. We will show later that both features affect the structure of the superconducting gap function. For band parameters from Table I,  $\Phi_{\text{cr}} \approx 7.6$  meV.

### B. X and Y pockets

The electron pockets are described by the band Hamiltonian  $H_{X/Y}$  [17,34,45,46]

$$H_{X/Y} = \psi_{X/Y}^\dagger \begin{pmatrix} A_{X/Y}^{(1)} & -iV_{X/Y} \\ iV_{X/Y} & A_{X/Y}^{(2)} \end{pmatrix} \psi_{X/Y}. \quad (8)$$

The diagonal elements are

$$A_{X/Y}^{(1)} = \frac{\mathbf{k}^2}{2m_1} - \mu_1 - \frac{a_1}{2} \mathbf{k}^2 \cos 2\theta_{X/Y} \pm \Phi_e, \quad (9)$$

$$A_{X/Y}^{(2)} = \frac{\mathbf{k}^2}{2m_3} - \mu_3 - \frac{a_3}{2} \mathbf{k}^2 \cos 2\theta_{X/Y}. \quad (10)$$

Here,  $\mathbf{k}$  is measured from  $X = (\pi, 0)$  for the X pocket and from  $Y = (0, \pi)$  for the Y pocket, and the upper (lower) sign corresponds to the X (Y) pocket.  $\theta_X$  ( $\theta_Y$ ) is the polar angle, measured with respect to the  $k_{x(y)}$  direction for the X (Y) electron pocket in the anticlockwise direction.  $\Phi_e$  is the electron nematic order defined as  $\Phi_e = \langle d_{xz,Y}^\dagger d_{xz,Y} - d_{yz,X}^\dagger d_{yz,X} \rangle$ . We choose  $\Phi_e < 0$  (opposite in sign to  $\Phi_h$ ). The off-diagonal term  $V_{X/Y}$  is defined as

$$V_X(k, \theta_X) = \sqrt{2}vk \sin \theta_X + \frac{p_1}{\sqrt{2}} k^3 \sin \theta_X (\sin^2 \theta_X + 3 \cos^2 \theta_X)$$

$$- \frac{p_2}{\sqrt{2}} k^3 \sin \theta_X \cos 2\theta_X, \quad (11)$$

$$V_Y(k, \theta_Y) = -V_X(k, \theta_Y). \quad (12)$$

TABLE II. Band parameters for the electron pocket.

$\mu_1$	$\mu_3$	$(2m_1)^{-1}$	$(2m_3)^{-1}$	$a_1$	$a_3$	$v$	$p_1$	$p_2$
19.9	39.4	1.4	186	136	-403	-122	-137	-11.7

The band parameters of Eq. (8) are listed in Table II. We borrowed the numbers from Refs. [3,10], where these parameters have been extracted from ARPES data.

Diagonalizing Eq. (8) near the X point, we find that there is a single band that crosses the Fermi level in both the tetragonal and the orthorhombic phase; see Figs. 3(c) and 3(d). The same holds near Y; see Figs. 3(e) and 3(f). We only consider these bands and neglect the ones that are located fully below  $E_F$ . The dispersions of the two relevant bands are

$$\xi_{X/Y} = \frac{A_{X/Y}^{(1)} + A_{X/Y}^{(2)}}{2} + \sqrt{\left(\frac{A_{X/Y}^{(1)} - A_{X/Y}^{(2)}}{2}\right)^2 + V_{X/Y}^2}, \quad (13)$$

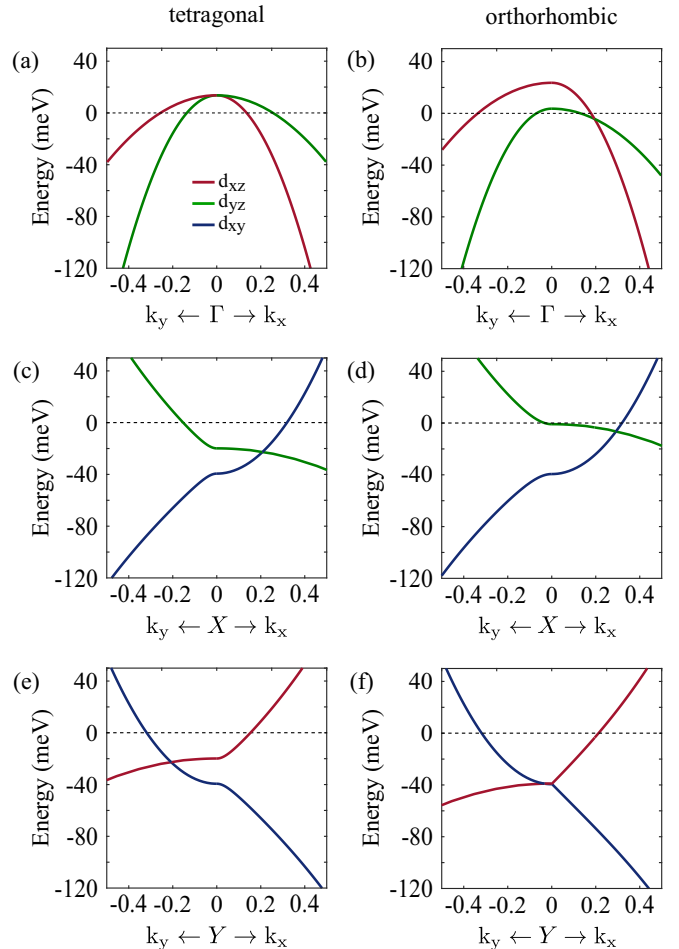


FIG. 3. Scenario A: Calculated band dispersion of the 1-Fe unit cell in tetragonal and orthorhombic phase, respectively, near (a), (b)  $\Gamma$ , (c), (d) X, and (e), (f) Y points of the BZ, respectively. Fitting parameters are taken from Refs. [3,10].

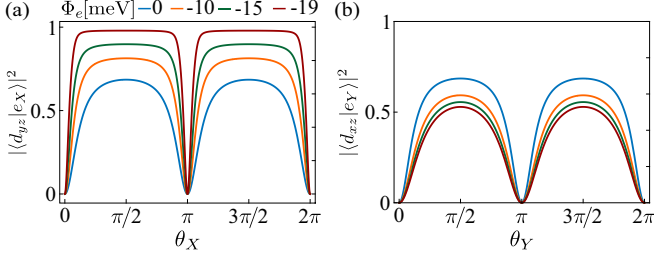


FIG. 4. The angular variation of orbital content  $|\langle d_{yz}|e_X\rangle|^2 = \cos^2 \phi_X$  on the  $X$  pocket (a) and  $|\langle d_{xz}|e_Y\rangle|^2 = \cos^2 \phi_Y$  on the  $Y$  pocket (b) for a set of  $\Phi_e$ .

and the band operators  $e_X$  and  $e_Y$ , in terms of which  $H_{X/Y} = \sum_{\mathbf{k},\sigma} \xi_{X/Y}(\mathbf{k}) e_{X/Y,\mathbf{k},\sigma}^\dagger e_{X/Y,\mathbf{k},\sigma}$ , are

$$e_X = -i \cos \phi_X d_{yz} + \sin \phi_X d_{xy}, \quad (14)$$

$$e_Y = i \cos \phi_Y d_{xz} + \sin \phi_Y d_{xy}, \quad (15)$$

where

$$\cos^2(\phi_{X/Y}) = \frac{1}{2} \left[ 1 + \frac{\frac{A_{X/Y}^{(1)} - A_{X/Y}^{(2)}}{2}}{\sqrt{\left(\frac{A_{X/Y}^{(1)} - A_{X/Y}^{(2)}}{2}\right)^2 + V_{X/Y}^2}} \right]. \quad (16)$$

The angular variation of the orbital  $d_{yz/xz}$  content,  $|\langle d_{yz/xz}|e_{X/Y}\rangle|^2 = \cos^2 \phi_{X/Y}$ , on the Fermi surface is plotted in Fig. 4. Because of  $C_4$  symmetry in the tetragonal phase,  $X$  and  $Y$  pockets have the same amount of  $d_{yz}$  and  $d_{xz}$  orbital content (blue lines in Fig. 4). With increasing  $\Phi_e$ , the  $X$  pocket becomes more of  $d_{yz}$  character and deforms into a peanut, while the  $Y$  pocket becomes more of  $d_{xy}$  character as its  $d_{xz}$  content decreases. For our band parameters, the  $X$  pocket splits into two smaller pockets once  $|\Phi_e| \geq 19.9$  meV (the short axis of the peanut becomes zero). Below, we limit  $\Phi_e$  to be smaller than this value.

### III. SUPERCONDUCTIVITY

#### A. Pairing interaction

The pairing interaction for the model with local fermion-fermion interaction in the band basis has been discussed previously [34,35]. We include the following components of the interaction Hamiltonian, relevant to the pairing: intra-orbital density-density interaction between fermions on the hole and electron pockets,  $U_{he}$ , and interorbital pair-hopping interaction between fermions on hole and electron pockets,  $J_{he}$ , and between the two electron pockets,  $J_{ee}$ . There are other pairing interactions, i.e., a repulsion within each pocket, but we restrict our consideration to these three as they are enhanced by magnetic fluctuations with momenta  $(0, \pi)$ ,  $(\pi, 0)$ , and  $(\pi, \pi)$ . The interaction Hamiltonian reads

$$\begin{aligned} H_{\text{int}} = & U_{he} \sum_{\mathbf{k}, \mathbf{k}', \mu} d_{\mu, \mathbf{k}, \uparrow}^\dagger d_{\mu, -\mathbf{k}, \downarrow}^\dagger d_{\mu, -\mathbf{k} + \mathbf{Q}_{\mu}, \downarrow} d_{\mu, \mathbf{k}' + \mathbf{Q}_{\mu}, \uparrow} \\ & + J_{he} \sum_{\mathbf{k}, \mathbf{k}', \mu \neq \nu} d_{\mu, \mathbf{k}, \uparrow}^\dagger d_{\mu, -\mathbf{k}, \downarrow}^\dagger d_{\nu, -\mathbf{k} + \mathbf{Q}_{\nu}, \downarrow} d_{\nu, \mathbf{k}' + \mathbf{Q}_{\nu}, \uparrow} \\ & + J_{ee} \sum_{\mathbf{k}, \mathbf{k}', \mu \neq \nu} d_{\mu, \mathbf{k} + \mathbf{Q}_{\mu}, \uparrow}^\dagger d_{\mu, -\mathbf{k} + \mathbf{Q}_{\mu}, \downarrow}^\dagger d_{\nu, -\mathbf{k}' + \mathbf{Q}_{\nu}, \downarrow} d_{\nu, \mathbf{k}' + \mathbf{Q}_{\nu}, \uparrow} \\ & + \text{H.c.} \end{aligned} \quad (17)$$

We consider only the pairing interaction involving  $d_{xz}$  and  $d_{yz}$  fermions, i.e., we assume that  $\mu, \nu \in \{xz, yz\}$ , and  $\mathbf{Q}_{xz} = (0, \pi)$ ,  $\mathbf{Q}_{yz} = (\pi, 0)$ . The restriction to  $d_{xz}$  and  $d_{yz}$  orbitals is justified as  $d_{xy}$ -fermions have a larger mass [38]. To convert the interaction Hamiltonian, Eq. (17), from the orbital to the band basis, we use

$$d_{xz, \mathbf{k}} = \sin \phi_h(\mathbf{k}) h_{\mathbf{k}}, \quad d_{xz, \mathbf{k} + \mathbf{Q}_{xz}} = \cos \phi_Y(\mathbf{k}) e_{Y, \mathbf{k}}, \quad (18)$$

$$d_{yz, \mathbf{k}} = \cos \phi_h(\mathbf{k}) h_{\mathbf{k}}, \quad d_{yz, \mathbf{k} + \mathbf{Q}_{yz}} = \cos \phi_X(\mathbf{k}) e_{X, \mathbf{k}}. \quad (19)$$

Substituting these into Eq. (17), we obtain the pairing interaction in the band basis,

$$\begin{aligned} H_{\text{pair}} = & \sum_{\mathbf{k}, \mathbf{p}} h_{\mathbf{k}, \uparrow}^\dagger h_{-\mathbf{k}, \downarrow}^\dagger \times [U_s (e_{X, -\mathbf{p}, \downarrow} e_{X, \mathbf{p}, \uparrow} \cos^2 \phi_X + e_{Y, -\mathbf{p}, \downarrow} e_{Y, \mathbf{p}, \uparrow} \cos^2 \phi_Y) + U_d \cos 2\phi_h (e_{X, -\mathbf{p}, \downarrow} e_{X, \mathbf{p}, \uparrow} \cos^2 \phi_X \\ & - e_{Y, -\mathbf{p}, \downarrow} e_{Y, \mathbf{p}, \uparrow} \cos^2 \phi_Y)] + J_{ee} \cos^2 \phi_X \cos^2 \phi_Y e_{X, \mathbf{k}, \uparrow}^\dagger e_{X, -\mathbf{k}, \downarrow}^\dagger e_{Y, -\mathbf{p}, \downarrow} e_{Y, \mathbf{p}, \uparrow} + \text{H.c.}, \end{aligned} \quad (20)$$

where  $U_s = \frac{U_{he} + J_{he}}{2}$  and  $U_d = \frac{U_{he} - J_{he}}{2}$  are  $s$ - and  $d$ -wave components of the pairing interaction between the hole and the electron pockets. We use  $\alpha = \frac{U_d}{U_s}$  to measure the relative strength of this part of the interaction in the  $s$ -wave and the  $d$ -wave channels.

#### B. Gap equation

We introduce the gap functions  $\Delta_h$  on the hole pocket and  $\Delta_X$  and  $\Delta_Y$  on the electron pockets. The equations for  $\Delta_h$ ,  $\Delta_X$ , and  $\Delta_Y$  are obtained by solving a  $3 \times 3$  matrix equation. We present the BCS gap equations in Appendix B, Eqs. (B1)–(B3). The solutions of these gap equations are

$$\Delta_h = \Delta_1 + \Delta_2 \cos 2\phi_h, \quad (21)$$

$$\Delta_X = \Delta_3 \cos^2 \phi_X, \quad (22)$$

$$\Delta_Y = \Delta_4 \cos^2 \phi_Y. \quad (23)$$

At  $T \approx T_c$ ,  $\Delta_i$  ( $i = 1, \dots, 4$ ) are the solutions of the matrix equation:

$$\begin{bmatrix} \Delta_1 \\ \Delta_2 \\ \Delta_3 \\ \Delta_4 \end{bmatrix} = \frac{1}{\lambda} \begin{bmatrix} 0 & 0 & -N_X \langle \cos^4 \phi_X \rangle & -N_Y \langle \cos^4 \phi_Y \rangle \\ 0 & 0 & -N_X \alpha \langle \cos^4 \phi_X \rangle & N_Y \alpha \langle \cos^4 \phi_Y \rangle \\ -N_h \langle 1 + \alpha \cos 2\phi_h \rangle & -N_h \langle \cos 2\phi_h + \alpha \cos^2 2\phi_h \rangle & 0 & -\frac{J_{ee}}{U_s} N_Y \langle \cos^4 \phi_Y \rangle \\ -N_h \langle 1 - \alpha \cos 2\phi_h \rangle & -N_h \langle \cos 2\phi_h - \alpha \cos^2 2\phi_h \rangle & -\frac{J_{ee}}{U_s} N_X \langle \cos^4 \phi_X \rangle & 0 \end{bmatrix} \begin{bmatrix} \Delta_1 \\ \Delta_2 \\ \Delta_3 \\ \Delta_4 \end{bmatrix}. \quad (24)$$

Here  $\lambda$  is the eigenvalue of the gap matrix defined as  $\frac{1}{\lambda} = U_s \ln(\frac{\Delta}{T})$ ,  $\langle A \rangle$  defines the angular average of  $A$  over the corresponding Fermi surface pocket, and  $N_X$ ,  $N_Y$ , and  $N_h$  are the densities of states for the  $X$ ,  $Y$ , and  $\Gamma$  pocket, respectively. In Figs. 5(a)–5(c), we show the variation of  $\langle \cos 2\phi_h \rangle$ ,  $\langle \cos^2 2\phi_h \rangle$ ,  $\langle \cos^4 \phi_X \rangle$ , and  $\langle \cos^4 \phi_Y \rangle$  as a function of the nematic order  $\Phi_{h,e}$ . We find that  $\langle \cos 2\phi_h \rangle$  and  $\langle \cos^2 2\phi_h \rangle$  exhibit a kink like nonanalyticity near  $\Phi_h = \Phi_{cr}$ . In the Appendix A we show that the singularities (nonanalyticities) are  $x \ln(x)$  and  $x^2 \ln(x)$ , where  $x = \Phi_h/\Phi_{cr} - 1$ . The densities of states also depend on  $\Phi_{h,e}$ , as we show in Fig. 5(d).

We numerically solve Eq. (24) and obtain  $T_c$  and find the gap structure  $\Delta = (\Delta_1, \Delta_2, \Delta_3, \Delta_4)$  for the leading superconducting instability. In the tetragonal phase,  $N_X = N_Y = N_e$  and  $\langle \cos 2\phi_h \rangle = \langle \cos 2\theta_h \rangle = 0$ . Then  $s^\pm$ -wave and  $d$ -wave pairing channels are decoupled. The eigenvalues of the gap matrix, Eq. (24), are

$$\lambda_s = \lambda_0 \left[ -\frac{J_{ee}}{U_s} + \sqrt{\left(\frac{J_{ee}}{U_s}\right)^2 + 8 \frac{N_h}{N_e \langle \cos^4 \phi_X \rangle}} \right], \quad (25)$$

$$\lambda_d = \lambda_0 \left[ \frac{J_{ee}}{U_s} + \sqrt{\left(\frac{J_{ee}}{U_s}\right)^2 + 4 \frac{N_h}{N_e \langle \cos^4 \phi_X \rangle} \alpha^2} \right], \quad (26)$$

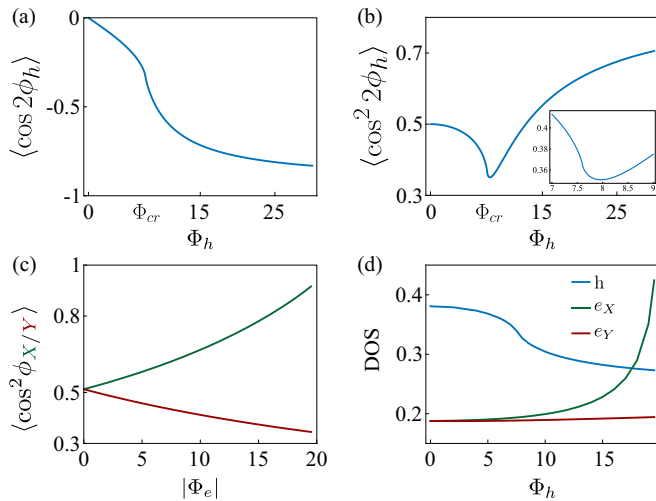


FIG. 5. Variation of the angular average of (a)  $\langle \cos 2\phi_h \rangle$ , (b)  $\langle \cos^2 2\phi_h \rangle$ , and (c)  $\langle \cos^2 \phi_X \rangle$  and  $\langle \cos^2 \phi_Y \rangle$  on the hole and the electron pockets with the nematic order  $\Phi_{h,e}$ . The inset in (b) shows the zoom-in view of  $\langle \cos^2 2\phi_h \rangle$  near  $\Phi_{cr}$ . The nonanalyticity is at  $\Phi_{cr} \approx 7.6$  meV. (d) Variations of the density of state (DOS) on different pockets with  $\Phi_h$ .

where  $\lambda_0 = \frac{N_e \langle \cos^4 \phi_X \rangle}{2}$ . For  $J_{ee} = 0$ , the gap function is either  $s$ -wave, for  $\alpha < \sqrt{2}$ , or  $d$ -wave, for  $\alpha > \sqrt{2}$ . For  $J_{ee} \neq 0$ , superconductivity is  $s$ -wave when

$$\frac{J_{ee}}{U_s} < \sqrt{\frac{N_h}{2N_e \langle \cos^4 \phi_X \rangle} \frac{(2 - \alpha^2)}{\sqrt{\alpha^2 + 2}}}. \quad (27)$$

The phase diagram for Eq. (27) is shown in Fig. 6. We next move to the nematic phase. Now  $\langle \cos 2\phi_h \rangle \neq 0$ , and both  $\Delta_1$  and  $\Delta_2$  are nonzero for any  $\alpha$  and  $J_{ee}$ .

To simplify the presentation, we neglect  $J_{ee}$ . Without nematicity, superconducting order is  $s$ -wave for  $\alpha < \sqrt{2}$  and  $\Delta_h = \Delta_1$ . At small  $\Phi$  (i.e., small  $\Phi_h$  and  $\Phi_e$ ),  $\phi_h \approx \theta_h$  and  $\Delta_2 \propto \Phi$ . This gives rise to  $\Phi \cos 2\theta_h$  angular variation of  $\Delta_h$ . If this was the only effect of nematicity, the angle variation would grow with  $\Phi$ , and  $\Delta_h$  would necessarily develop a deep minima and then gap nodes. However, as  $\Phi$  increases,  $\phi_h$  deviates from  $\theta_h$  due to orbital transmutation, and at large  $\Phi$  it becomes  $\pi/2$  almost everywhere on the hole pocket. Then the  $\Delta_2 \cos 2\phi_h$  term becomes angle-independent, and the gap function on the hole pocket recovers a pure  $s$ -wave form. Besides, due to the same orbital transmutation, the magnitude  $\Delta_2$  becomes a nonlinear function of  $\Phi$  and does not necessarily exceed  $\Delta_1$  even at large  $\Phi$ .

A similar situation holds if  $\alpha > \sqrt{2}$ , when the superconducting order without nematicity is  $d$ -wave,  $\Delta_h = \Delta_2 \cos 2\theta_h$ . At a small  $\Phi$ , the key effect of nematicity is an admixture of  $\Delta_1$ . At large  $\Phi$ ,  $\theta_h \rightarrow \phi_h \approx \pi/2$ , and the nodes disappear.

The questions, which we address below, are (i) whether for  $\alpha < \sqrt{2}$  the nodes in  $\Delta_h$  develop at intermediate  $\Phi_h$ , and (ii) how the nodes in  $\Delta_h$  disappear for  $\alpha > \sqrt{2}$  as  $\Phi_h$  increases. To address these issues, we solve the gap equations for different  $\alpha$  at various  $\Phi_h$  and  $\Phi_h/\Phi_e$ . We show the results in Figs. 7–11. Before we discuss these results, several general observations are in order. According to Eq. (22),  $\Delta_h$  has a

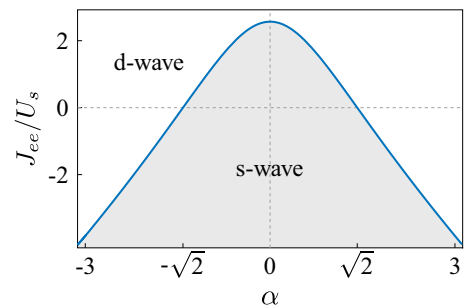


FIG. 6. Regions of  $s$ -wave and  $d$ -wave superconductivity according to the solution of Eq. (27) for different  $\alpha$  and  $J_{ee}$  in the absence of nematicity.

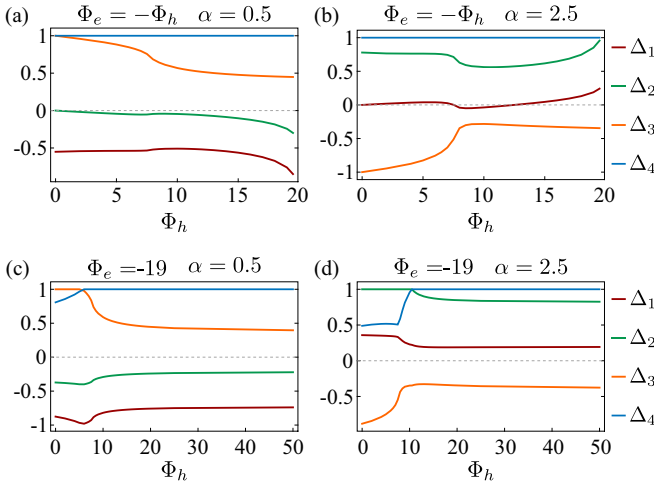


FIG. 7. Variations of the gap amplitudes  $\Delta = (\Delta_1, \Delta_2, \Delta_3, \Delta_4)$  with the nematic order  $\Phi_{e,h}$  and interaction ratio  $\alpha$  for (a)  $\alpha = 0.5$ ,  $\Phi_h = -\Phi_e$ ; (b)  $\alpha = 2.5$ ,  $\Phi_h = -\Phi_e$ ; (c)  $\alpha = 0.5$ ,  $\Phi_e = -19$  meV; and (d)  $\alpha = 2.5$ ,  $\Phi_e = -19$  meV.

node at an angle  $\theta_0$  if

$$\cos 2\phi_h(\theta_0, \Phi_h) = -\frac{\Delta_1}{\Delta_2}. \quad (28)$$

The ratio  $\Delta_2/\Delta_1$  depends on  $\Phi_h$ ,  $\Phi_e$ , and  $\alpha$ . Obviously, the nodes are possible only if  $|\Delta_2/\Delta_1| > 1$ . Shrinking the angular variation of  $\cos 2\phi_h$  at  $\Phi_h > \Phi_{cr}$  puts additional restriction on  $\Delta_2/\Delta_1$  for the nodes to appear. Further, the number of possible nodes changes between  $\Phi_h < \Phi_{cr}$  and  $\Phi_h > \Phi_{cr}$ . In the first case, the gap functions at  $\theta = 0$  and  $\frac{\pi}{2}$  are  $\Delta_1 + \Delta_2$  and  $\Delta_1 - \Delta_2$ , respectively. When  $|\Delta_2/\Delta_1| > 1$ , the two have opposite signs, hence there have to be an odd number of nodes between 0 and  $\frac{\pi}{2}$ ; the total number of nodes is then 4, 12, 20, ... . For  $\Phi_h > \Phi_{cr}$ ,  $\Delta_h(\theta)$  at  $\theta = 0$  and  $\pi/2$  become the same  $\Delta_1 - \Delta_2$  due to orbital transmutation. Then, there have to be an even number of nodes between 0 and  $\pi/2$ , hence the total number of nodes is 0, 8, 16, ... .

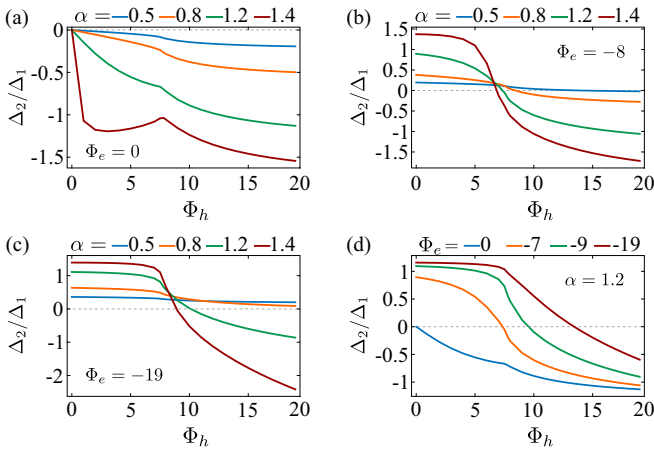


FIG. 8. The variation of  $\Delta_2/\Delta_1$  with  $\Phi_h$  for different interaction ratios  $\alpha$  for a fixed electron nematic order (a)  $\Phi_e = 0$  meV, (b)  $\Phi_e = -8$  meV, and (c)  $\Phi_e = -19$  meV. In (d) we fix  $\alpha = 1.2$  and plot  $\Delta_2/\Delta_1$  with  $\Phi_h$  for different values of electron nematic order  $\Phi_e$ .

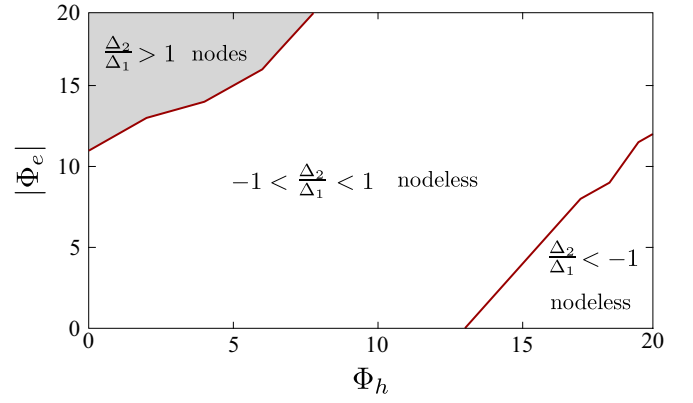


FIG. 9. The variation of  $\Delta_2/\Delta_1$  as a function of  $\Phi_h$  and  $\Phi_e$ . We set  $\alpha = 1.2$  in this plot.

In our case, we find (see the Appendix C for details)

$$\frac{\Delta_2}{\Delta_1} = 2\alpha \frac{g + \alpha(\cos 2\phi_h)}{(1 - \alpha^2(\cos^2 2\phi_h)) + D}, \quad (29)$$

where

$$g = g(\Phi_e) = \frac{N_X(\cos^4 \phi_X) - N_Y(\cos^4 \phi_Y)}{N_X(\cos^4 \phi_X) + N_Y(\cos^4 \phi_Y)} \quad (30)$$

and

$$D = [4\alpha^2((\cos 2\phi_h)^2 - (\cos^2 2\phi_h))(1 - g^2) + (1 + 2g\alpha(\cos 2\phi_h) + \alpha^2(\cos^2 2\phi_h))^2]^{1/2}. \quad (31)$$

The function  $g(\Phi_e)$  measures the asymmetry between  $X$  and  $Y$  pockets at a nonzero  $\Phi_e$ . We find that it increases roughly linearly with  $|\Phi_e|$ .

We now discuss the results. In Figs. 7(a) and 7(c) we show  $\Delta_i$  for  $\alpha = 0.5$ , and in Figs. 7(b) and 7(d) we show  $\Delta_i$  for  $\alpha = 2.5$  when the primary order is  $s$ -wave and  $d$ -wave, respectively. We see that for  $\alpha = 0.5$ , the magnitude of the  $s$ -wave component  $\Delta_1$  far exceeds  $\Delta_2$  of the  $d$ -wave component, i.e., the gap remains an  $s$ -wave with a small admixture of a  $d$ -wave. For  $\alpha = 2.5$ , the situation is opposite—the gap

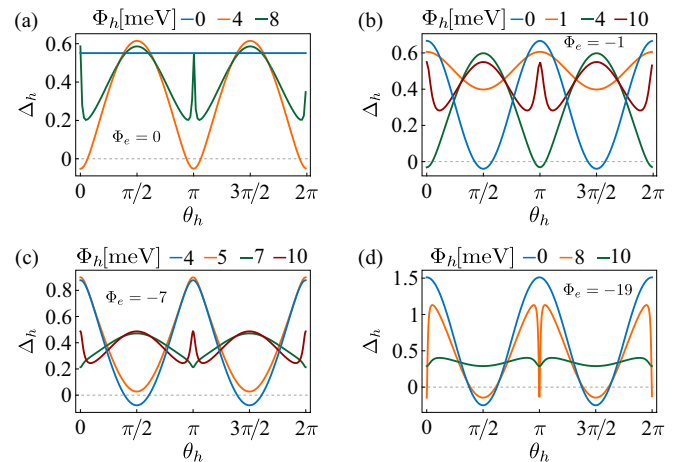


FIG. 10. The angular variation of  $\Delta_h(\theta_h)$  with  $\theta_h$  for various values of  $\Phi_h$  at (a)  $\Phi_e = 0$  meV, (b)  $\Phi_e = -1$  meV, (c)  $\Phi_e = -7$  meV, and (d)  $\Phi_e = -19$  meV. We set  $\alpha = 1.4$ .

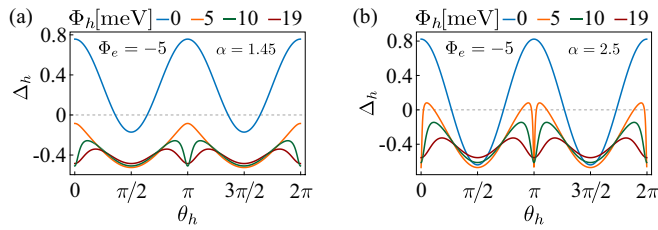


FIG. 11. Angular variation of  $\Delta_h(\theta_h)$  at selected values of  $\Phi_h$  for (a)  $\alpha = 1.45$  and (b)  $\alpha = 2.5$ . We set  $\Phi_e = -5$  meV.

remains predominantly  $d$ -wave with a small admixture of an  $s$ -wave. In both cases, therefore, the effect of nematicity is rather weak, even when  $\Phi_h$  is large.

In Fig. 8, we plot  $\Delta_2/\Delta_1$  as a function of  $\Phi_h$  for various  $\Phi_e$  and  $\alpha < \sqrt{2}$ . We see that when  $\alpha$  is not close to  $\sqrt{2}$ , then  $|\Delta_2/\Delta_1| < 1$  for any  $\Phi_h$  and  $\Phi_e$ . As a consequence, there are no nodes in the gap function. This agrees with Fig. 7. However, for  $\alpha \leq \sqrt{2}$ , we find intervals of  $\Phi_h < \Phi_{cr}$ , where  $|\Delta_2/\Delta_1| > 1$ . This holds, e.g., for  $\alpha = 1.4$  and  $\Phi_e = 0$  [dark red curve in Fig. 8(a)]. By our generic reasoning, there must be four nodes. The same holds for the same  $\alpha$  and sizable  $\Phi_e$  [see Figs. 8(b) and 8(c)]. The only difference is that for  $\Phi_e = 0$ , the four nodes are near the  $k_x$ -direction, while for sizable  $\Phi_e$  they are near the  $k_y$ -direction.

Next, we see from Fig. 8 that the ratio  $|\Delta_2/\Delta_1|$  evolves around  $\Phi_h = \Phi_{cr}$  and even changes sign for sizable  $\Phi_e$ . For larger  $\Phi_h$  we again have  $|\Delta_2/\Delta_1| > 1$  for  $\alpha \leq \sqrt{2}$ . However, this no longer guarantees the existence of the nodes as by our general reasoning above their number can be zero. We will see that this is what happens—the nodes do not develop despite  $|\Delta_2/\Delta_1| > 1$  because  $\phi_h$  clusters around  $\pi/2$ .

In Fig. 9 we mark the boundaries of  $|\Delta_2/\Delta_1|$  on the  $(\Phi_h, \Phi_e)$  plane at a fixed  $\alpha = 1.2$ . The area of the “corner” regions, where  $|\Delta_2/\Delta_1| > 1$ , increases when  $\alpha$  approaches  $\sqrt{2}$ . As we mentioned, the nodes only develop in the left upper grayish colored corner, where  $\Phi_h < \Phi_{cr}$ . In Fig. 10 we plot the gap function  $\Delta_h(\theta_h)$ . We find four different scenarios in which nodes can appear/disappear when one varies  $\Phi_h$  at a fixed value of  $\Phi_e$  and  $\alpha$  slightly below critical  $\sqrt{2}$ . Here, we further set  $\alpha = 1.4$ .

(i) In Fig. 10(a) we set  $\Phi_e = 0$ . There are no nodes at  $\Phi_h = 0$ , in agreement with Fig. 8(a). At  $\Phi_h \approx 1$  meV, four nodes appear near the  $k_x$ -direction. They exist up to  $\Phi_h \leq \Phi_{cr}$  and disappear at larger  $\Phi_h$ . In the node count, the number of nodes changes with  $\Phi_h$  as  $0 \rightarrow 4 \rightarrow 0$ .

(ii) In Fig. 10(b) we set  $\Phi_e = -1$  meV. In this case, there are four nodes near the  $k_y$ -direction already for  $\Phi_h = 0$ . As  $\Phi_h$  increases, the four nodes disappear at  $\Phi_h \sim 1$  meV due to nonmonotonic behavior of  $\Delta_2/\Delta_1$ , as in Figs. 8(b) and 8(c). As  $\Phi_h$  increases further, four nodes reappear, now near the  $k_x$ -direction, at  $\Phi_h \sim 3$  meV. These nodes then disappear at  $\Phi_h \leq \Phi_{cr}$ . In this case, the number of nodes changes with  $\Phi_h$  as  $4 \rightarrow 0 \rightarrow 4 \rightarrow 0$ .

(iii) In Fig. 10(c) we set  $\Phi_e = -7$  meV. In this case, at small  $\Phi_h$  there are four nodes near the  $k_y$ -direction. These nodes disappear at some  $\Phi_h \leq \Phi_{cr}$ . In this case, the number of nodes changes with  $\Phi_h$  as  $4 \rightarrow 0$ .

(iv) In Fig. 10(d) we set  $\Phi_e = -19$  meV. In this case, there are four nodes near the  $k_y$ -direction for all  $\Phi_h \leq \Phi_{cr}$ . For  $\Phi_h > \Phi_{cr}$ , the number of nodes first increases from four to eight, because the gap function along the  $k_x$ - and the  $k_y$ -direction becomes nearly the same and has to cross zero twice. As  $\Phi_h$  increases further, the eight nodes disappear due to the clustering of  $\phi_h$  near  $\pi/2$ . In this case, the number of nodes changes with  $\Phi_h$  as  $4 \rightarrow 8 \rightarrow 0$ . For  $\alpha > \sqrt{2}$ , superconducting order in the tetragonal phase is  $d$ -wave with four nodes on the hole pocket. With increasing nematic order, the nodes disappear due to orbital transmutation either because  $\Delta_1$  becomes larger than  $\Delta_2$  or  $\Delta_2$  remains larger than  $\Delta_1$ , but  $\phi_h$  clusters around  $\pi/2$ . In Fig. 11 we show the results for  $\Delta_h$  at two values of  $\alpha > \sqrt{2}$ . For  $\alpha = 1.45$ , the nodes  $\Delta_h$  disappear because  $\Delta_1$  becomes larger than  $\Delta_2$ . This happens at  $\Phi_h < \Phi_{cr}$ , i.e., well before  $\phi_h$  starts clustering near  $\pi/2$ . In this case, the number of nodes changes with  $\Phi_h$  as  $4 \rightarrow 0$ . For  $\alpha = 2.5$ ,  $\Delta_2$  remains larger than  $\Delta_1$ , and the nodes disappear at  $\Phi_h > \Phi_{cr}$  due to clustering of  $\phi_h$ . We see from the figure that in this case the number of nodes changes with  $\Phi_h$  as  $4 \rightarrow 8 \rightarrow 0$  (4 on a blue line, 8 on an orange line, and 0 on green and red lines). A nodeless gap deep in the orthorhombic phase for  $\alpha > \sqrt{2}$  is consistent with RPA calculations of Ref. [11].

Note that the results for a nonzero  $J_{ee}$  are quite similar; only the value of  $\alpha$  near which the system develops nodes coming out of an  $s$ -wave superconductor at  $\Phi = 0$  shifts from  $\alpha = \sqrt{2}$ .

### C. Temperature dependence of the gap

In this section, we obtain the temperature dependence of  $\Delta_i(T)$  near the superconducting transition. We will use the result for  $\Delta_i(T)$  in the next section, where we compute the jump of the specific heat at  $T_c$ . We assume that the ratios  $\Delta_i/\Delta_j$  do not change substantially with temperature. This relies on the assumption that the dimensional coupling constants (the products of the interband/intraband interaction and the corresponding densities of states in the normal state) are temperature-independent at  $T \leq T_c$ . Accordingly, we parametrize four gap functions as

$$\Delta(T) = \Delta_0(T)(\Delta_1, \Delta_2, \Delta_3, \Delta_4) = \Delta_0(T)\mathbf{\Delta}, \quad (32)$$

where  $\mathbf{\Delta} = (\Delta_1, \Delta_2, \Delta_3, \Delta_4)$  are the same (up to an overall factor) as we obtained in Sec. III B by solving the linearized gap equations (24). We normalize  $\mathbf{\Delta}$  by setting its largest component equal to 1. To simplify the presentation, we again first assume  $J_{ee} = 0$  and then present the results for a nonzero  $J_{ee}$ .

The nonlinear equation for the gap on the hole pocket is

$$\begin{aligned} & \Delta_1 + \Delta_2 \cos 2\phi_h \\ &= - \left[ \Delta_3 (U_s + U_d \cos 2\phi_h) \int_{\mathbf{p}} \frac{\tanh(\frac{E_x}{2T})}{2E_x} \cos^4 \phi_X \right. \\ & \quad \left. + \Delta_4 (U_s - U_d \cos 2\phi_h) \int_{\mathbf{p}} \frac{\tanh(\frac{E_y}{2T})}{2E_y} \cos^4 \phi_Y \right], \quad (33) \end{aligned}$$

where  $E_X = \sqrt{\xi_x^2 + \Delta_3^2 \Delta_0^2(T)}$  and  $E_Y = \sqrt{\xi_y^2 + \Delta_4^2 \Delta_0^2(T)}$ . Multiplying Eq. (33) by  $\Delta_1 + \Delta_2 \cos 2\phi_h$ , averaging over the hole Fermi surface pocket, and expanding the right-hand side

to order  $\Delta_0^2(T)$  as

$$\begin{aligned} & \int_{\mathbf{p}} \frac{\tanh(\frac{E_{X/Y}}{2T})}{2E_{X/Y}} \cos^4 \phi_{X/Y}(\mathbf{p}) \\ &= N_{X/Y} \left( \ln \frac{\Lambda}{T} \langle \cos^4 \phi_{X/Y} \rangle - K \Delta_3^2 \frac{\Delta_0^2}{T_c^2} \langle \cos^8 \phi_{X/Y} \rangle \right) \\ & \quad + O(\Delta_0^4), \end{aligned} \quad (34)$$

where  $K = \frac{7\xi(3)}{8\pi^2}$ , we obtain

$$\begin{aligned} & N_h \ln \frac{\Lambda}{T_c} \langle (\Delta_1 + \Delta_2 \cos 2\phi_h)^2 \rangle \\ &= \ln \frac{\Lambda}{T} [N_X \Delta_3^2 \langle \cos^4 \phi_X \rangle + N_Y \Delta_4^2 \langle \cos^4 \phi_Y \rangle] \\ & \quad - K \frac{\Delta_0(T)^2}{T_c^2} [N_X \Delta_3^4 \langle \cos^8 \phi_X \rangle + N_Y \Delta_4^4 \langle \cos^8 \phi_Y \rangle]. \end{aligned} \quad (35)$$

$$\Delta_0(T)^2 = \frac{T_c(T_c - T)}{K} \frac{N_X \Delta_3^2 \langle \cos^4 \phi_X \rangle + N_Y \Delta_4^2 \langle \cos^4 \phi_Y \rangle + 2 \frac{J_{ee}}{\lambda} N_X N_Y \Delta_3 \Delta_4 \langle \cos^4 \phi_X \rangle \langle \cos^4 \phi_Y \rangle}{N_X \Delta_3^4 \langle \cos^8 \phi_X \rangle + N_Y \Delta_4^4 \langle \cos^8 \phi_Y \rangle + \frac{J_{ee}}{\lambda} N_X N_Y \Delta_3 \Delta_4 (\Delta_3^2 \langle \cos^8 \phi_X \rangle \langle \cos^4 \phi_Y \rangle + \Delta_4^2 \langle \cos^8 \phi_Y \rangle \langle \cos^4 \phi_X \rangle)}, \quad (38)$$

where  $\lambda$  is the largest eigenvalue of Eq. (24). We note in passing that the temperature variation of the gaps ratio is generally stronger if the pairing is mediated by dynamical collective excitations, e.g., spin fluctuations, as in this case the couplings are renormalized below  $T_c$  due to the feedback from superconductivity.

#### IV. SPECIFIC HEAT

In this section, we examine the specific heat jump at  $T_c$  and its band-resolved compositions as a function of nematicity for scenarios A and B. In the mean-field approximation, the specific heat is the sum of contributions from  $\Gamma$ ,  $X$ , and  $Y$  pockets:

$$C_v = \sum_{i=h,X,Y} \int_{\mathbf{k}} \left( \frac{E_i^2(\mathbf{k})}{2T^2} - \frac{1}{4T} \frac{\partial |\Delta_i(\mathbf{k})|^2}{\partial T} \right) \frac{1}{\cosh^2(\frac{E_i(\mathbf{k})}{2T})}. \quad (39)$$

The first term on the right-hand side of Eq. (39) is the normal state contribution at  $T = T_c + 0^+$ . Evaluating the  $k$ -integral, we obtain

$$C_v = \frac{2}{3} \pi^2 T_c (N_h + N_X + N_Y). \quad (40)$$

The second term on the right-hand side of Eq. (39) accounts for the jump of  $\Delta C_v$  at  $T_c$ . It is equal to

$$\begin{aligned} \Delta C_v &= -\frac{1}{4T_c} \sum_{i=h,X,Y} \int_{\mathbf{k}} \frac{1}{\cosh^2(\frac{\xi_i(\mathbf{k})}{2T_c})^2} \frac{d}{dT} \Delta_i(\theta)^2 \\ &= -\sum_{i=h,X,Y} N_i \int_0^{2\pi} \frac{d\theta}{2\pi} \frac{d}{dT} \Delta_i(\theta)^2. \end{aligned} \quad (41)$$

Multiplying Eq. (B4) by  $\Delta_1 + \Delta_2 \cos 2\phi_h$ , averaging over the hole Fermi surface pocket, and using Eqs. (B5) and (B6), we obtain the relation

$$\begin{aligned} & N_h \langle (\Delta_1 + \Delta_2 \cos 2\phi_h)^2 \rangle \\ &= (N_X \Delta_3^2 \langle \cos^4 \phi_X \rangle + N_Y \Delta_4^2 \langle \cos^4 \phi_Y \rangle). \end{aligned} \quad (36)$$

Approximating  $\ln \frac{\Lambda}{T} \approx \ln \frac{\Lambda}{T_c} + \frac{T_c - T}{T_c}$  and using Eq. (36), we obtain from (35)

$$\Delta_0(T)^2 = \frac{T_c(T_c - T)}{K} \frac{N_X \Delta_3^2 \langle \cos^4 \phi_X \rangle + N_Y \Delta_4^2 \langle \cos^4 \phi_Y \rangle}{N_X \Delta_3^4 \langle \cos^8 \phi_X \rangle + N_Y \Delta_4^4 \langle \cos^8 \phi_Y \rangle}. \quad (37)$$

We recall that  $\Delta_3$  and  $\Delta_4$  are functions of  $\Phi_h$ ,  $\Phi_e$ , and  $\alpha$ . For  $J_{ee} \neq 0$ , the same procedure yields

Substituting the results for the gap functions, we find that

$$\begin{aligned} \Delta C_v &= -\frac{d}{dT} \Delta_0(T)^2 [N_h \langle (\Delta_1 + \Delta_2 \cos 2\phi_h)^2 \rangle \\ & \quad + N_X \Delta_3^2 \langle \cos^4 \phi_X \rangle + N_Y \Delta_4^2 \langle \cos^4 \phi_Y \rangle] \\ &= \Delta C_v^h + \Delta C_v^X + \Delta C_v^Y. \end{aligned} \quad (42)$$

Setting  $J_{ee} = 0$  and using Eq. (36), we find that  $\Delta C_v^h = \Delta C_v^X + \Delta C_v^Y$ . Using Eqs. (36), (37), and (42), we find

$$\frac{\Delta C_v}{C_v} = 1.43 \frac{2N_h^2 \langle \Delta_h(\theta)^2 \rangle^2}{N(N_X \Delta_3^4 \langle \cos^8 \phi_X \rangle + N_Y \Delta_4^4 \langle \cos^8 \phi_Y \rangle)}, \quad (43)$$

where 1.43 is the BCS result for a single band superconductor, and  $N = N_h + N_X + N_Y$ . Without a nematic order, the ratio would be

$$\left( \frac{\Delta C_v}{C_v} \right)_{\Phi=0} = 1.43 \frac{2}{1 + \frac{N_h}{2N_e}} \frac{\langle \cos^4 \phi_X \rangle^2}{\langle \cos^8 \phi_X \rangle}. \quad (44)$$

If the electron pockets would consist solely of  $d_{xz}$  and  $d_{yz}$  fermions, we would obtain  $\Delta C_v/C_v|_{\Phi=0} = 2.86/[1 + N_h/(2N_e)]$ . For the parameters from Tables I and II, this yields  $\Delta C_v/C_v|_{\Phi=0} = 1.42$ . In the presence of the  $d_{xy}$  orbital, however,  $\Delta C_v/C_v|_{\Phi=0} \approx 1.09$ . The smallness comes from the fact that the relatively heavy  $d_{xy}$  band contributes to  $C_v(T)$  in the normal state, but not to  $\Delta C_v$ . This is similar to the case of  $\text{KFe}_2\text{As}_2$  (Ref. [38]).

#### A. Specific heat jump at $T_c$ for scenario A

The effect of nematicity on the specific heat jump is involved because  $N_i$ ,  $c_i$ , and the coherence factors  $\cos \phi_i$  all vary with it. In Fig. 12, we plot  $\Delta C_v/C_v$  as a function of  $\Phi_h$  for various values of  $\Phi_e$  and representative  $\alpha = 0.5$  and 2.5, chosen to be smaller and larger than  $\sqrt{2}$ . For  $\alpha = 0.5$ , we

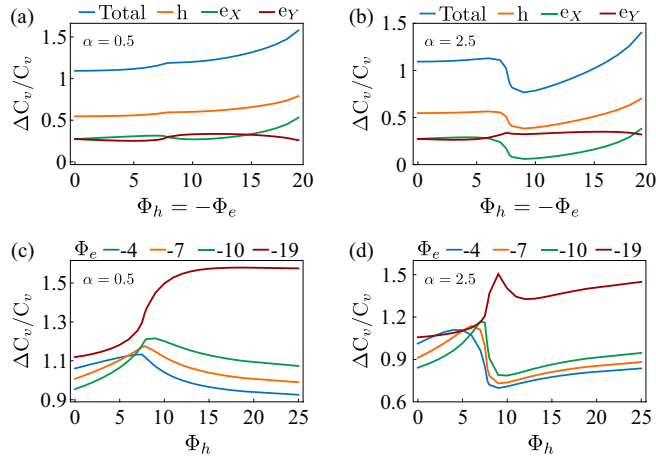


FIG. 12. The variation of the scaled specific heat jump  $\frac{\Delta C_v}{C_v}$  with hole nematic order  $\Phi_h$  for (a), (c)  $\alpha = 0.5$  and (b), (d)  $\alpha = 2.5$ . We set  $\Phi_e = -\Phi_h$  in (a) and (b). In (c) and (d), we choose a set of values for  $\Phi_e = \{-4, -7, -10, -19\}$  meV.

expect from Eq. (43) that  $\Delta C_v/C_v \approx \Delta_1^4$ , and we verified that the behavior of  $\Delta C_v/C_v$  matches the behavior of  $\Delta_1^4$  with  $\Delta_1$  from Fig. 7(a).

For  $\alpha = 2.5$ , we expect  $\Delta C_v/C_v \sim \Delta_2^4$ , and the behavior of  $\Delta C_v/C_v$  matches the behavior of  $\Delta_2^4$  with  $\Delta_2$  from Fig. 7(b). In both cases, we see that  $\Delta C_v/C_v$  is generally around 1, but it increases with  $\Phi_h$ . Viewed as a function of  $\Phi_h$ ,  $\Delta C_v/C_v$  displays a kink like nonanalyticity at  $\Phi_h = \Phi_{cr}$  and, moreover, is nonmonotonic at  $\alpha = 2.5$ . The nonmonotonic behavior for this  $\alpha$  is clearly visible in Fig. 12(d), where we plot  $\Delta C_v/C_v$  versus  $\Phi_h$  for various  $\Phi_e$ . Figure 12(c) shows that it also holds at  $\alpha = 0.5$  for large enough  $|\Phi_e|$ . At large  $|\Phi_e|$  and even larger  $\Phi_h$ ,  $\Delta C_v/C_v$  saturates. The reason is that for such  $\Phi$ , the  $Y$  pocket is mostly of  $d_{xy}$  character and the  $X$  pocket is mostly of  $d_{yz}$  character, hence  $\langle \cos^a \phi_Y \rangle \ll 1$  and  $\langle \cos^a \phi_X \rangle \approx 1$ , where  $a = 4, 8$ . Then  $\Delta C_v/C_v \sim N_X/(N_h + N_X + N_X)$ , and  $N_X$  is the largest; see Fig. 5(d). Note that for large  $|\Phi_e| = 19$  meV,  $\Delta C_v/C_v$  is 1.5–1.6.

For  $\alpha \approx \sqrt{2}$ , the behavior of  $\Delta C_v/C_v$  versus  $\Phi_h$  is intermediate between the ones at  $\alpha = 0.5$  and 2.5.

We also plot in Figs. 12(a) and 12(b) the band-resolved contributions from hole and electron pockets. We see that the largest contribution to the jump comes from the hole pocket.  $\Delta C_v^h/C_v$  is nonanalytic at  $\Phi_{cr}$  and gives rise to nonanalyticity in the full  $\Delta C_v/C_v$ .

### B. Specific heat jump at $T_c$ for scenario B

Below we present the results for the specific heat jump and its decomposition into contributions from different bands for scenario B, when there is additional contribution  $\Phi_{xy}$ , Eq. (2). This contribution splits the dispersions of  $d_{xy}$  fermions on the  $X$  and  $Y$  pockets. We choose the sign and magnitude of  $\Phi_{xy}$  such that the bottom of the  $Y$  band moves above the chemical potential, i.e., the  $Y$  pocket disappears in the nematic phase. To simplify calculations, we adopt the ‘‘antisymmetric approach’’ of Ref. [11] and introduce  $\Phi_{xy}$  nematic order only for  $d_{xy}$  fermions on the  $Y$  pocket, as  $2\Psi_Y \Phi_{xy} \Psi_Y$  with  $\Psi_Y$  from Eq. (8). Appropriate parameters to fit the band structure, available from ARPES experiments, in this scenario are given

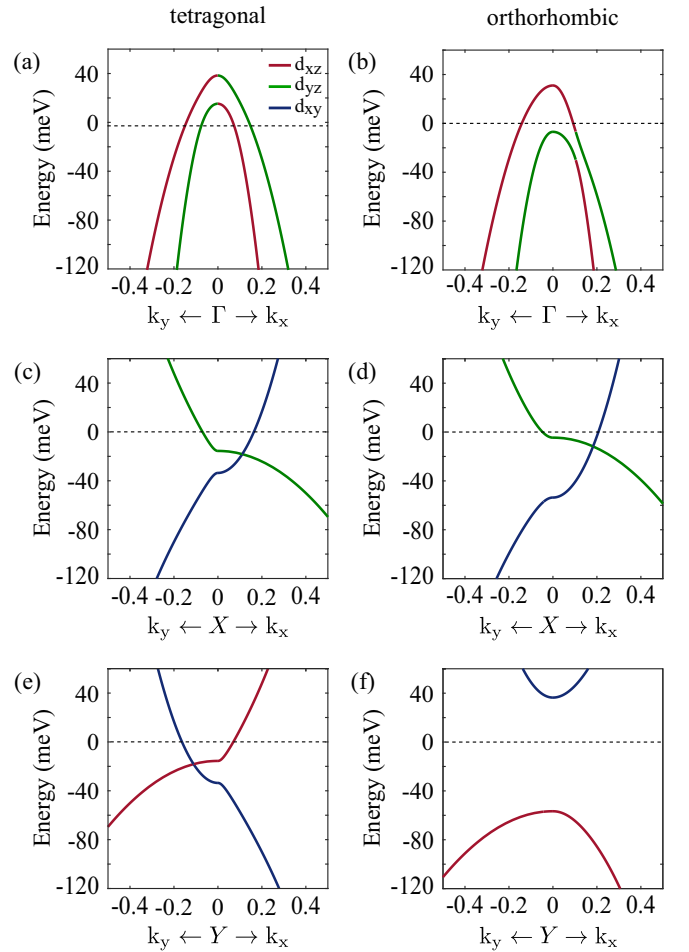


FIG. 13. Scenario B: Calculated band dispersion of the 1-Fe unit cell in tetragonal and orthorhombic phase, respectively, near (a), (b)  $\Gamma$ , (c), (d)  $X$ , and (e), (f)  $Y$  point. Fitting parameters are taken from Ref. [11]. Note that the  $d_{xy}$  dominated  $Y$ -band is fully located above the Fermi level in (f).

in the supplementary material of Ref. [11], and they yield the Fermi surface shown in Fig. 1(d) and in the right inset in Fig. 14(c). The corresponding band dispersions at the  $\Gamma$ ,  $X$ , and  $Y$  points are shown in Fig. 13.

We solve the full nonlinear gap equations (B1)–(B3), substitute the results into Eq. (39), and obtain the specific heat.

In Fig. 14(a) we show the total specific heat  $C_V$  (solid-blue) as well as the band-resolved contributions from the  $\Gamma$ ,  $X$ , and  $Y$  pockets (solid yellow, green, and orange, respectively). For definiteness we set  $\Phi_{xy} = 45$  meV,  $\alpha = 0.5$ , and  $J_{eh} = J_{ee}$  ( $=U_{eh}/3$ ). We adjusted  $U_{eh}$  to match experimental  $T_c \sim 10$  K. Observe that both the  $\Gamma$  and  $X$  pockets contribute substantially to the specific heat jump, with the contribution from the  $Y$  pocket almost vanishing. The largest contribution comes from the  $X$  pocket. This differs from the result for scenario A, but the difference is largely due to different parameters, as we verified.

A more substantial difference is actually for the specific heat in the normal state. In scenario A,  $d_{xy}$  fermions from both  $X$  and  $Y$  pockets contribute to  $C_v(T)$  above  $T_c$ . In scenario B,  $d_{xy}$  fermions from  $Y$  are gapped, and only  $d_{xy}$  fermions from  $X$  contribute. As a result, the normal state  $C_v(T)$  is reduced

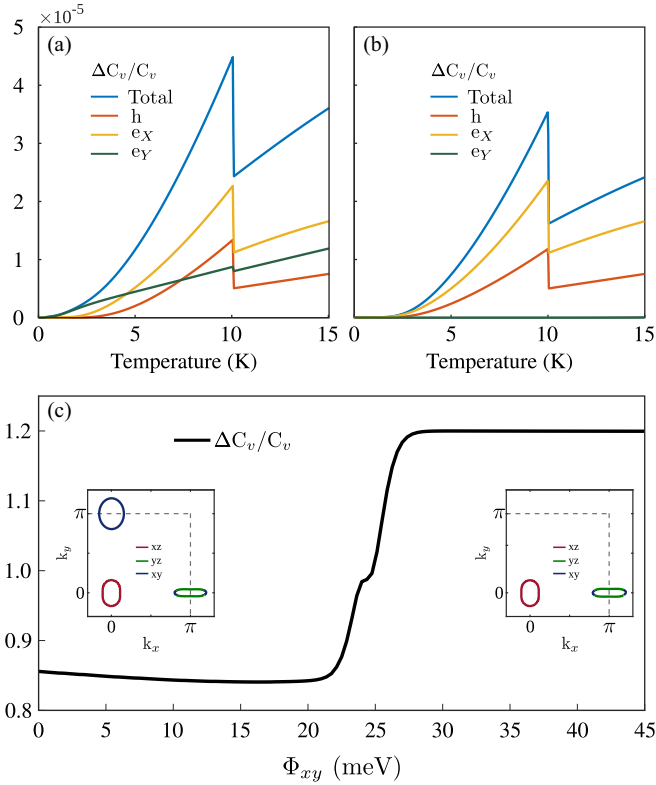


FIG. 14. The total and band-resolved specific heat calculated for (a) scenario A ( $\Phi_{xy} = 0$ ) and (b) scenario B ( $\Phi_{xy} = 45$  meV); (c)  $\Delta C_v/C_v$  as a function of  $\Phi_{xy}$ . For the small (large)  $\Phi_{xy}$  scenario, A (B) is valid. Left inset: Fermi surface for  $\Phi_{xy} = 0$ . Right inset: Fermi surface for  $\Phi_{xy} = 45$  meV.

in scenario B compared to A, while  $\Delta C_v$  at  $T_c$  remains the same as only  $d_{xz}$  and  $d_{yz}$  fermions contribute to the jump. As a consequence,  $\Delta C_v/C_v$  is larger in scenario B than in scenario A. We show this explicitly where we plot  $\Delta C_v/C_v$  as a function of  $\Phi_{xy}$ , which drives the system between scenario A and scenario B. We see that  $\Delta C_v/C_v$  is roughly a constant at small  $\Phi_{xy}$  when scenario A is valid. It then rapidly increases and saturates at a larger value at large  $\Phi_{xy}$  when scenario B is valid.

### C. Comparison between scenarios A and B and experiments

Specific heat measurements in FeSe [39–43,47–51] consistently reveal that  $\Delta C_v/C_v \approx 1.65$ . This is larger than the BCS result for a single band superconductor,  $\Delta C_v/C_v \approx 1.43$ . A larger  $\Delta C_v/C_v$  is often associated with the effects beyond BCS [52,53]. However, earlier works [54–59] have found that in a multiband system,  $\Delta C_v/C_v$  can be either larger or smaller than the BCS value already within BCS approximation. In our analysis, we obtain  $\Delta C_v/C_v$  around 1 in scenario A for small  $\Phi_e$  and  $\Phi_h$ , but larger  $\Delta C_v/C_v \sim 1.5$ – $1.6$  for larger  $\Phi_h \sim |\Phi_e| \leq 20$  meV. Within scenario B,  $\Delta C_v/C_v$  is always larger than in scenario A because the normal state contribution is smaller. Then the experimental  $\Delta C_v/C_v \sim 1.65$  can be reproduced already at smaller  $\Phi_{h,e}$ . In summary, the specific heat jump can be reproduced within both scenarios, but the parameter space is somewhat larger in scenario B. We also note

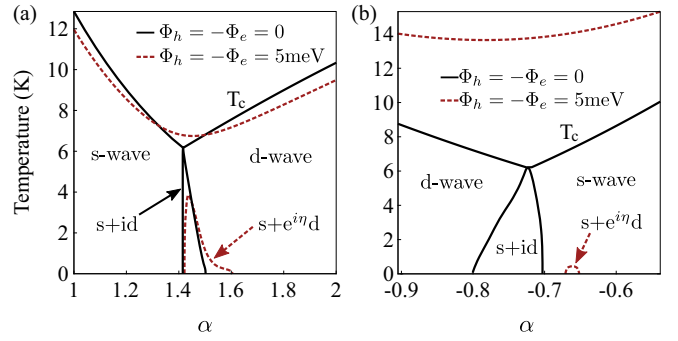


FIG. 15. Regions of the mixed  $s + e^{i\eta}d$  order in the tetragonal and orthorhombic phases in the  $(T, \alpha)$  plane. In (a) we set  $J_{ee} = 0$  and  $J_{eh} < 0$  to bring  $\alpha = (U_{eh} - J_{eh})/(U_{eh} + J_{eh})$  close to  $\sqrt{2}$ . In (b) we set  $J_{ee} = J_{eh} > 0$ . A  $d$ -wave order develops when  $J_{eh}/U_{eh}$  is larger than a certain number. For our parameter, the mixed phase is located near  $\alpha \sim -0.7$ . The shrinking of the range of  $s + e^{i\eta}d$  order with nematicity is stronger in (b) than in (a).

that the pocket sizes in scenario B are somewhat smaller compared to those in scenario A, which leads to some quantitative differences in the phase diagram in Fig. 6, mainly affecting the terms in the square root in Eq. (27). More specifically, both scenarios predict similar results for the angular dependence of the gap at the outer hole pocket, shown in Fig. 9, but they differ in their predictions for the electron pockets. This has been discussed previously in Refs. [25,34].

### V. SPECIFIC HEAT NEAR A POSSIBLE TRANSITION INTO AN $s + e^{i\eta}d$ STATE

In this section, we consider the possibility of a second superconducting transition in FeSe, caused by a transformation of the  $s + d$  state into the  $s + e^{i\eta}d$  state. Such an instability may arise near the point where the pairing interaction is attractive in both  $s$ -wave and  $d$ -wave channels, with comparable magnitudes. The parameter range of  $s + e^{i\eta}d$  has been previously analyzed in Ref. [35], assuming that the nematic order is weak. Here we do not keep  $\Phi$  small and include into consideration orbital transmutation in the nematic phase. We identify the parameter range, where  $s + e^{i\eta}d$  order emerges.

To analyze the transition to the  $(s + e^{i\eta}d)$ -wave state, we numerically solve the full nonlinear gap equations (B1)–(B3), including both  $s$ -wave and  $d$ -wave harmonics. We show our results in Fig. 15. In panel (a), we assume  $J_{ee} = 0$  and vary the parameter  $\alpha$ , which drives the system from  $s$ - to  $d$ -wave symmetry at  $\alpha \approx \sqrt{2}$ . In panel (b) we set  $J_{ee} = J_{eh}$ ; in this case, the transition from  $s$ - to  $d$ -wave is at negative  $\alpha \sim -0.7$ . The black curves in Fig. 15 are the results for  $\Phi = 0$ . In both panels, there is a sizable range of  $s + id$  order, sandwiched between pure  $s$ -wave and  $d$ -wave states. This is consistent with Ref. [35]. For a finite nematic order, the gap function in the mixed state is  $s + e^{i\eta}d$ , where  $0 \leq \eta \leq \frac{\pi}{2}$ . The results for  $\Phi \neq 0$  show that nematicity generally suppresses the width of the  $s + e^{i\eta}d$  region, but the suppression is far stronger for  $J_{ee} = J_{eh}$  [panel (b)] than for  $J_{ee} = 0$  [panel (a)]. The reason why a nematic order is unfavorable for the  $s + e^{i\eta}d$  state is again orbital transmutation: as we said, a nematic order makes pockets “mono-orbital” and therefore favors  $s$ -wave

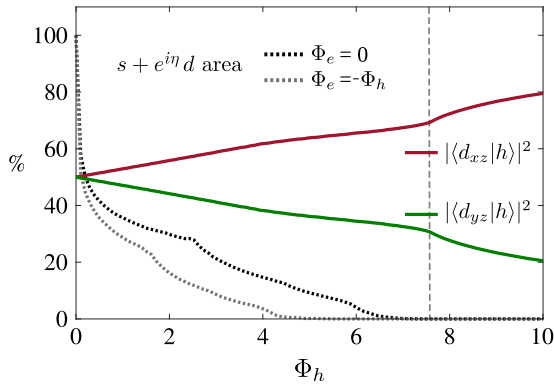


FIG. 16. The size of the  $s + e^{in}d$  region (black) and the percentage of  $d_{xz}$  and  $d_{yz}$  orbital content at the hole pocket (red and green), vs  $\Phi_h$ . The black-dashed line is for  $\Phi_e = 0$ , while the gray-dashed line is for  $\Phi_e = -\Phi_h$ .

pairing. Consequently, the region where  $s$ - and  $d$ -wave pairing channels are nearly degenerate gets suppressed. We illustrate this in Fig. 16, where we plot the area of the  $s + e^{in}d$  region, normalized to its value in the tetragonal state, and the difference in the orbital content on the hole pocket, both versus  $\Phi_h$ . We see that the area of the mixed range shrinks and vanishes when  $\Phi_h$  reaches  $\Phi_{cr}$ .

Specific heat measurements on FeSe in Refs. [39–42] reported two jumps at  $T_c = 8$  K and  $T^* \sim 1$  K. The jump at  $T_c$  clearly indicates the transition to the superconducting phase. In Ref. [35] it was argued that the jump at  $T^* = 1$  K might be explained by the transition into the  $s + e^{in}d$  phase. Our results show that this is possible, but unlikely as the parameter range when  $s + e^{in}d$  order develops is quite narrow.

We also note in passing that in panel (b) of Fig. 15,  $T_c$  goes up at a nonzero  $\Phi$ , despite the fact that a nematic order is generally believed to be a competitor to superconductivity. This happens because  $J_{eh}$  is the dominant component of the pairing interaction, and  $J_{eh}$  couples  $d_{xz}$  fermions on the  $\Gamma$  pocket to  $d_{yz}$  fermions on the  $X$  pocket. The spectral weight of both fermions gets enhanced by sign-changing  $d_{xz/yz}$  nematicity, and this enhances  $T_c$ . For the case in panel (a), the dominant interaction is  $U_{eh}$ , which couples  $d_{xz}$  ( $d_{yz}$ ) orbitals at  $\Gamma$  with  $d_{xz}$  ( $d_{yz}$ ) orbitals at  $Y$  ( $X$ ). In the nematic phase,  $d_{xz}$  ( $d_{yz}$ ) weight is enhanced (reduced) at  $\Gamma$  but reduced (enhanced) at  $Y$  ( $X$ ). As a consequence,  $T_c$  is weakly affected by nematicity.

## VI. CONCLUSIONS

In this paper, we presented an in-depth analysis of the superconducting gap function and the specific heat of a multi-orbital metal, like FeSe, which first develops a nematic order and then undergoes a transition into a superconducting state, which coexists with nematicity. We considered two scenarios: scenario A, in which nematic order develops between  $d_{xz}$  and  $d_{yz}$  orbitals on hole and electron pockets ( $\Phi_h$  and  $\Phi_e$ ), and scenario B, in which there is an additional component of the nematic order for  $d_{xy}$  fermions on the two electron pockets ( $\Phi_{xy}$ ).

We specifically addressed three questions. The first one is the angular dependence of the gap. Here we analyzed the competition between the two effects. One is the nematicity-induced  $s$ - $d$  mixture, which necessarily induces angular variation of the gap function even if the superconducting state is an  $s$ -wave without nematicity. Another one is orbital transmutation of low-energy excitations in the nematic state. This effect tends to make Fermi surface pockets mono-orbital and thus favors an angle-independent gap function. We analyzed the crossover from initial  $s$ - $d$  mixing to the eventual angle-independent gap, and we argued that the most likely scenario for stronger  $s$ -wave attraction in the tetragonal phase is a gap function with no nodes, while for stronger  $d$ -wave attraction the four nodes from  $d$ -wave order disappear once nematic order exceeds a certain threshold. However, in a parameter range where  $s$ -wave and  $d$ -wave interactions have comparable strength, we find more involved crossovers in which, e.g., the number of nodal points goes from zero to a finite number and then back to zero, or when the number of nodal points goes from four to eight and then to zero.

The second question that we addressed is the behavior of a specific heat in a nematic superconductor. For this, we solved the nonlinear gap equation, obtained the forms of the gaps below  $T_c$ , and used them to compute the specific heat  $C_v(T)$ . We analyzed the evolution of  $C_v(T)$  with the nematic order in both scenario A and scenario B. Here our key result is the specific heat jump at  $T_c$ :  $\Delta C_v/C_v$ . We found that  $\Delta C_v/C_v$  is around 1 in the tetragonal phase for parameters appropriate for FeSe. The magnitude of  $\Delta C_v/C_v$  increases with the nematic order and saturates at  $\Delta C_v/C_v \sim 1.5$ – $1.6$ . This is quite consistent with the experimental result for FeSe,  $\Delta C_v/C_v \sim 1.65$  (Refs. [39–43,47–51]). The values of  $\Phi_{h,e}$  required to reach saturation are smaller in scenario B as in this scenario the normal state  $C_v(T)$  is smaller as it assumes that the  $Y$  pocket disappears because of sizable  $\Phi_{xy}$ .

The third question that we addressed is a potential transition at  $T_{c1} < T_c$  from an  $s + d$  state to an  $s + e^{in}d$  state that breaks time-reversal symmetry. Such a transition was suggested [35] as a possible explanation of the experiments [39–43], which observed a second jump of  $C_v(T)$  at  $T^* \sim 1$  K, well below  $T_c \sim 8.5$  K. At small  $\Phi_{h,e}$ , previous study found [35] that the parameter range where the  $s + e^{in}d$  state develops at  $T \rightarrow 0$  is quite sizable. We analyzed larger  $\Phi_{h,e}$  and found that the range shrinks due to orbital transmutation, which acts against competition between  $s$ - and  $d$ -pairing. We expect that the measurements of the gap function and specific heat in doped FeSe $_{1-x}$ S $_x$  or FeSe $_{1-x}$ Te $_x$ , where the amount of nematic order varies with  $x$ , could verify the presence of the  $s + e^{in}d$  state.

## ACKNOWLEDGMENTS

We thank Rafael Fernandes, Thierry Klein, and Hai-Hu Wen for useful conversations. The work by K.R.I. and A.V.C. was supported by the U.S. Department of Energy, Office of Science, Basic Energy Sciences, under Award No. DE-SC0014402. The work of J.B. and I.M.E. was supported by a joint NSFC-DFG grant (ER 463/14-1).

**APPENDIX A: SINGULARITIES IN THE HOLE COHERENCE FACTOR**

In this Appendix, we compute  $\langle \cos 2\phi_h \rangle$  and  $\langle \cos^2 2\phi_h \rangle$  as a function of  $\Phi_h$ , and we show, respectively, that they exhibit an  $x \ln |x|$ - and  $x^2 \ln |x|$ -type nonanalyticity near the critical nematic strength  $\Phi_{\text{cr}}$  (defined below). Using Eqs. (5) and (7),

$$\cos 2\phi_h = \frac{bx_f(\theta) \cos(2\theta_h) - \Phi_h}{\frac{x_f(\theta)}{m_h} - \mu_h} = m_h b \frac{bx_f(\theta) \cos(2\theta_h) - \Phi_h}{bx_f(\theta) - \Phi_{\text{cr}}}, \quad (\text{A2})$$

where  $\Phi_{\text{cr}} = \mu_h m_h b$  is the critical nematic strength where the orbital order in the  $k_x$ -direction changes from  $d_{yz}$  to  $d_{xz}$  on the hole pocket. We set  $m_h b = t$  for convenience, and for our model parameters from Table I,  $t \approx 0.5$ . We find the functional form of  $bx_f(\theta)$  from the band dispersion Eq. (5) as

$$bx_f(\theta) = \frac{\Phi_{\text{cr}} - t^2 \Phi_h \cos 2\theta + \sqrt{(\Phi_{\text{cr}} - t^2 \Phi_h \cos 2\theta)^2 - (1 - t^2)(\Phi_{\text{cr}}^2 - \Phi_h^2 t^2)}}{1 - t^2}. \quad (\text{A3})$$

In the limit where nematic order is small, i.e.,  $\Phi_h \ll \Phi_{\text{cr}}$ , we can expand Eqs. (A3) and (A1) in  $\frac{\Phi_h}{\Phi_{\text{cr}}} \ll 1$ , which yields

$$\langle \cos 2\phi_h \rangle_{\text{FS}} = -\frac{1-t}{2} \left( \frac{\Phi_h}{\Phi_{\text{cr}}} \right) - \frac{1-t^2}{16} \left( \frac{\Phi_h}{\Phi_{\text{cr}}} \right)^3 + O(\Phi_h^5), \quad (\text{A4})$$

$$\langle \cos^2 2\phi_h \rangle_{\text{FS}} = \frac{1}{2} - t \frac{1-t}{4} \left( \frac{\Phi_h}{\Phi_{\text{cr}}} \right)^2 + O(\Phi_h^4). \quad (\text{A5})$$

In the limit when  $\Phi_h \approx \Phi_{\text{cr}}$ , we find from Eq. (A3) precisely at  $\Phi_h = \Phi_{\text{cr}}$

$$bx_f^{\text{cr}}(\theta, \Phi_{\text{cr}}) = \Phi_{\text{cr}} + \Phi_{\text{cr}} f(\theta), \quad (\text{A6})$$

where

$$f(\theta) = \frac{2t^2 \sin^2(\theta) + 2t |\sin(\theta)| \sqrt{1 - t^2 \cos^2(\theta)}}{1 - t^2}. \quad (\text{A7})$$

Then,

$$\begin{aligned} \cos 2\phi_h &= t \frac{[\Phi_{\text{cr}} + \Phi_{\text{cr}} f(\theta)] \cos(2\theta) - \Phi_{\text{cr}}}{\Phi_{\text{cr}} + \Phi_{\text{cr}} f(\theta) - \Phi_{\text{cr}}} \\ &= t \left[ -\frac{1}{f(\theta)} + \cos(2\theta) \left( 1 + \frac{1}{f(\theta)} \right) \right] \\ &= t \left[ \cos(2\theta) - 2 \frac{\sin^2(\theta)}{f(\theta)} \right]. \end{aligned} \quad (\text{A8})$$

From Eq. (A8), we find that near the  $k_x$ -axis,  $\cos 2\phi_h$  approaches the value  $t$ , while it is undefined in the  $k_x$ -direction. We will show later  $\cos 2\phi_h(0) = \text{sgn}(\Phi_{\text{cr}} - \Phi_h)$ ,

$$\lim_{\theta \rightarrow 0} \cos 2\phi_h(\theta)_{\Phi_{\text{cr}}} = t. \quad (\text{A9})$$

Averaging  $\cos 2\phi_h$  and  $\cos^2 2\phi_h$  over the angle  $\theta$ , we get

$$\begin{aligned} \langle \cos 2\phi_h \rangle &= t \langle \cos(2\theta) \rangle - 2t \left\langle \frac{\sin^2(\theta)}{f(\theta)} \right\rangle \\ &= \frac{t}{2} - \frac{\sqrt{1-t^2}}{\pi} - \frac{\arcsin(t)}{\pi t} \\ &\approx -0.32, \end{aligned} \quad (\text{A10})$$

we write  $\cos 2\phi_h$  on the Fermi surface as

$$\cos 2\phi_h = \frac{b \frac{\mathbf{k}_F(\theta)^2}{2} \cos(2\theta_h) - \Phi_h}{\frac{\mathbf{k}_F(\theta)^2}{2m_h} - \mu_h}. \quad (\text{A1})$$

Here,  $\mathbf{k}_F(\theta)$  is the Fermi radius at an angle  $\theta$ . We define  $\frac{\mathbf{k}_F^2}{2} = x_f(\theta)$  for convenience, and we write

$$\begin{aligned} \langle \cos^2 2\phi_h \rangle &= t^2 \left\langle \cos^2 2\theta + 4 \frac{\sin^4 \theta}{f(\theta)^2} - 4 \frac{\cos 2\theta \sin^2 \theta}{f(\theta)} \right\rangle \\ &= \frac{t[2(2-2t^2)\sqrt{1-t^2} + \pi t(2+t^2)] - 2 \arcsin t}{4\pi t^2} \\ &\approx 0.36. \end{aligned} \quad (\text{A11})$$

Next we assume  $\Phi_h = \Phi_{\text{cr}} + \delta$  and show how  $\langle \cos 2\phi_h \rangle$  and  $\langle \cos^2 2\phi_h \rangle$  depend on  $\delta$ . Using Eq. (A3), we show

$$bx_f(\theta, \delta) = \frac{\Phi_{\text{cr}}[1 - t^2 \cos(2\theta)] - \delta t^2 \cos(2\theta) + \sqrt{B}}{1 - t^2}, \quad (\text{A12})$$

where

$$\begin{aligned} B &= 4\Phi_{\text{cr}}^2 t^2 [1 - t^2 \cos^2(\theta)] \sin^2(\theta) + \delta^2 t^2 \\ &\quad - 4\delta^2 t^4 \sin^2(\theta) \cos^2(\theta) \\ &\quad + 4\delta t^2 \Phi_{\text{cr}} \sin^2(\theta) [1 - 2t^2 \cos^2(\theta)]. \end{aligned} \quad (\text{A13})$$

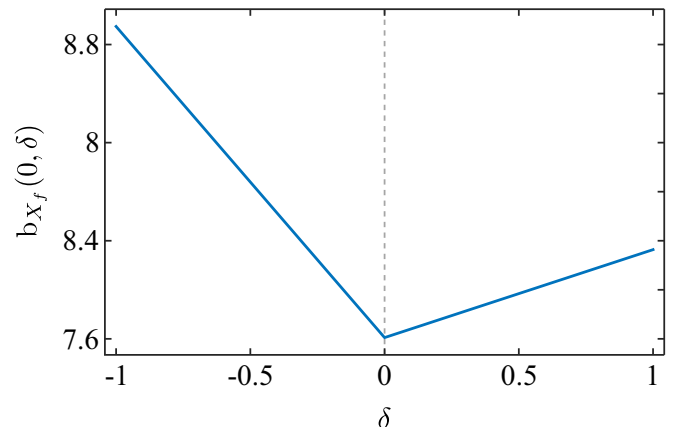


FIG. 17.  $bx_f(0, \delta)$  as function of  $\delta$ .

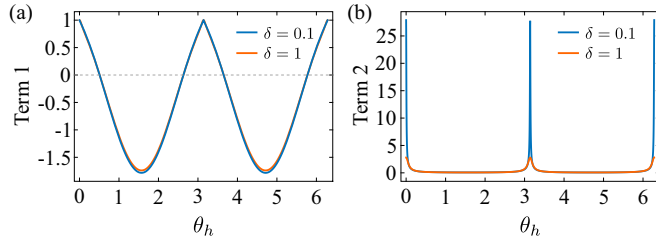


FIG. 18. We plot both of the integrands of Eq. (A16) as a function of  $\theta$  for  $\delta = 0.1$  and 1.

At  $\theta = 0, \pi$ ,  $bx_f(0, \delta)$  has a  $|\delta|$ -type nonanalyticity as we find from Eq. (A12)

$$bx_f(0, \delta) = \Phi_{\text{cr}} + \frac{t|\delta|}{1 + t \operatorname{sgn}(\delta)} \quad (\text{A14})$$

and plot in Fig. 17. As a result, we find

$$\begin{aligned} \cos 2\phi_h(0) &= t \frac{bx_f(0, \delta) - \Phi_{\text{cr}} - \delta}{bx_f(0, \delta) - \Phi_{\text{cr}}} \\ &= t \left( 1 - \frac{\delta}{bx_f(0, \delta) - \Phi_{\text{cr}}} \right) \\ &= t \left( 1 - \frac{\delta(1 - t^2)}{|\delta|t - \delta t^2} \right) \\ &= -\operatorname{sgn}(\delta). \end{aligned} \quad (\text{A15})$$

Next, we move to calculate  $\langle \cos 2\phi_h \rangle$ ,

$$\begin{aligned} \langle \cos 2\phi_h \rangle &= t \left\langle \frac{bx_f(\theta, \delta) \cos(2\theta) - \Phi_{\text{cr}}}{bx_f(\theta, \delta) - \Phi_{\text{cr}}} \right\rangle \\ &= t \left\langle \frac{bx_f(\theta, \delta) \cos(2\theta) - \Phi_{\text{cr}} - \delta}{bx_f(\theta, \delta) - \Phi_{\text{cr}}} \right\rangle \\ &= t \left\langle \underbrace{\frac{bx_f(\theta, \delta) \cos(2\theta) - \Phi_{\text{cr}}}{bx_f(\theta, \delta) - \Phi_{\text{cr}}}}_{\text{Term 1}} \right\rangle \\ &\quad - \delta t \left\langle \underbrace{\frac{1}{bx_f(\theta, \delta) - \Phi_{\text{cr}}}}_{\text{Term 2}} \right\rangle. \end{aligned} \quad (\text{A16})$$

We claim that the second blue underbraced term in Eq. (A16) contains the nonanalytic behavior of  $\langle \cos 2\phi_h \rangle$ ,

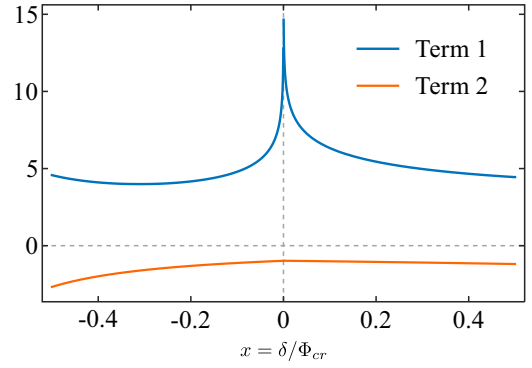


FIG. 19. Terms 1 and 2 according to Eq. (A21) as a function of  $x = \delta/\Phi_{\text{cr}}$ .

because, as  $\delta \rightarrow 0$ , the denominator diverges at  $\theta = 0$  and  $\pi$ ; see Fig. 18(b). The first underbraced term in Eq. (A16) is almost independent of variations in  $\delta$ , as can be seen in Fig. 18(a). Hence, we approximate the first term of Eq. (A16) by setting  $\delta = 0$ , and we recover the result of Eq. (A10).

To calculate the second term, we rewrite the denominator to separate the singular from the regular part,

$$\begin{aligned} bx_f(\theta, \delta) - \Phi_{\text{cr}} &= bx_f(\theta, \delta) - bx_f(0, \delta) + bx_f(0, \delta) - \Phi_{\text{cr}} \\ &= \frac{t|\delta|}{1 + t \operatorname{sgn}(\delta)} + [bx_f(\theta, \delta) - bx_f(0, \delta)]. \end{aligned} \quad (\text{A17})$$

We again approximate that  $[bx_f(\theta, \delta) - bx_f(0, \delta)]$  does not change much with  $\delta$ . So we write it as

$$bx_f(\theta, \delta) - bx_f(0, \delta) \approx bx_f(\theta, 0) - bx_f(0, 0) = \phi_{\text{cr}} f(\theta). \quad (\text{A18})$$

Then, the nonanalytic contribution of  $\langle \cos 2\phi_h \rangle$  is

$$\begin{aligned} \langle \cos 2\phi_h \rangle &= -\delta \left\langle \frac{1}{\Phi_{\text{cr}} f(\theta) + \frac{t|\delta|}{1 + t \operatorname{sgn}(\delta)}} \right\rangle \\ &= -x \left\langle \frac{1}{f(\theta) + A(x)} \right\rangle, \end{aligned} \quad (\text{A19})$$

where  $x = \frac{\delta}{\Phi_{\text{cr}}}$ , and

$$A(x) = t \frac{|x|}{1 + t \operatorname{sgn}(x)}. \quad (\text{A20})$$

We perform the integration over  $\theta$  in Eq. (A19), and we obtain

$$\langle \cos 2\phi_h \rangle = -2x \left[ \underbrace{\frac{\arccos(t)}{A(x) - 1}}_{\text{Term 1}} + \underbrace{\frac{2 - A(x)}{1 - A(x)} \frac{\sqrt{1 - t^2}}{\sqrt{[2 - A(x)]^2 t^2 - A(x)^2}} \tanh^{-1} \left( \frac{\sqrt{[2 - A(x)]^2 t^2 - A(x)^2}}{[2 - A(x)]t} \right)}_{\text{Term 2}} \right]. \quad (\text{A21})$$

As  $\delta \rightarrow 0$ , the first term of Eq. (A21) inside the parentheses approaches a finite value  $[-\arccos(t)]$ , while the second term blows up because of the  $\tanh^{-1}$  function (see Fig. 19). We neglect the regular part, and we expand the second term around  $x = 0$  to find the nonanalytic component, which is of  $|x| \ln(|x|)$  form,

$$\langle \cos 2\phi_h \rangle \propto -2x \left( 2 + t \frac{|x|}{1 + t \operatorname{sgn}(x)} \right) \left( \frac{1}{2t} + \frac{|x|}{4[1 + t \operatorname{sgn}(x)]} \right) [c - \ln(|x|)] \propto |x| \ln(|x|). \quad (\text{A22})$$

Next, we compute  $\langle \cos^2 2\phi_h \rangle$  in the following way:

$$\begin{aligned} \langle \cos^2 2\phi_h \rangle &= t^2 \left\langle \frac{bx_f(\theta, \delta) \cos(2\theta) - \Phi_{cr}}{bx_f(\theta, \delta) - \Phi_{cr}} \right\rangle^2 \\ &= t^2 \left[ \left\langle \frac{[bx_f(\theta, \delta) \cos(2\theta) - \Phi_{cr}]^2}{[bx_f(\theta, \delta) - \Phi_{cr}]^2} \right\rangle + \delta^2 \left\langle \frac{1}{[bx_f(\theta, \delta) - \Phi_{cr}]^2} \right\rangle - 2\delta \left\langle \frac{[bx_f(\theta, \delta) \cos(2\theta) - \Phi_{cr}]}{[bx_f(\theta, \delta) - \Phi_{cr}]^2} \right\rangle \right]. \end{aligned} \quad (\text{A23})$$

The first term of Eq. (A23) contains no singularity and gives the  $\delta = 0$  contribution to  $\langle \cos^2 2\phi_h \rangle$ . To calculate the singularity present in the second term, we approximate the denominator as we did in Eq. (A17). We further approximate the function  $f(\theta)$  near  $\theta = 0$ , where the nonanalyticity is located, and we find

$$f(\theta) = \frac{2t}{\sqrt{1-t^2}} (\theta + A_2 \theta^2 + O(\theta^3)), \quad (\text{A24})$$

where  $A_2 = \frac{t}{\sqrt{1-t^2}}$ . Using Eq. (A24), we calculate the second term of Eq. (A23) as

$$t^2 \delta^2 \left\langle \frac{1}{[bx_f(\theta, \delta) - \Phi_{cr}]^2} \right\rangle = (1-t^2) x^2 \int_0^{\pi/2} \frac{1}{[\theta + A_2 \theta^2 + A_0(x)]^2}. \quad (\text{A25})$$

We define  $A_0(x) = \frac{\sqrt{1-t^2}}{2} A(x)$ . Equation (A25) can be computed exactly, and it is equal to

$$x^2 \left\{ \frac{\pi}{A_0(x)[4A_0(x) + \pi(2 + A_2\pi)]} - \frac{\pi(1 + A_2\pi)}{A_0(x)V(x)^2[4A_0(x) + \pi(2 + A_2\pi)]} - 4 \frac{A_2}{V(x)^3} \left[ \arctan\left(\frac{1}{V(x)}\right) - \arctan\left(\frac{1 + A_2\pi}{V(x)}\right) \right] \right\}. \quad (\text{A26})$$

We define  $V(x) = \sqrt{-1 + 4A_2A_0(x)}$ . When  $x \rightarrow 0$ ,  $V(x) \rightarrow i$ . The first and second terms of Eq. (A26) are regular. To identify the nonanalytic behavior of the third term, we use the following identity, and we expand  $V(x)$  up to linear order in  $x$ :

$$\arctan(z) = -\frac{i}{2} \ln\left(\frac{1+iz}{1-iz}\right), \quad (\text{A27})$$

$$V(x) = i \left( 1 - t^2 \frac{|x|}{1 + t \operatorname{sgn}(x)} \right) = i\tilde{V}(x), \quad (\text{A28})$$

where  $\tilde{V}(x) = 1 - t^2 \frac{|x|}{1 + t \operatorname{sgn}(x)}$ . Using Eqs. (A27) and (A28), we find that

$$\arctan\left(\frac{1}{V(x)}\right) = -\frac{i}{2} \ln\left(\frac{\tilde{V}(x)+1}{\tilde{V}(x)-1}\right) \propto \ln\left(\frac{t^2|x|}{1 + t \operatorname{sgn}(x)}\right). \quad (\text{A29})$$

Equation (A29) shows that the most singular correction of Eq. (A26) is of the form  $x^2 \ln(|x|)$ . Finally, we write the last term of Eq. (A23) in the following way to show that it is also singular of the form  $x \ln(x)$ :

$$\delta \left\langle \frac{[bx_f(\theta, \delta) \cos(2\theta) - \Phi_{cr}]}{[bx_f(\theta, \delta) - \Phi_{cr}]^2} \right\rangle = \delta \left\langle \frac{[bx_f(\theta, \delta)(1 - 2\sin^2\theta) - \Phi_{cr}]}{[bx_f(\theta, \delta) - \Phi_{cr}]^2} \right\rangle = \delta \left\langle \frac{1}{[bx_f(\theta, \delta) - \Phi_{cr}]} \right\rangle - 2\delta \left\langle \frac{[bx_f(\theta, \delta) \sin^2\theta]}{[bx_f(\theta, \delta) - \Phi_{cr}]^2} \right\rangle. \quad (\text{A30})$$

We show that the first term is singular of the form  $x \ln(|x|)$ . We assume that the second term is not singular because of the  $\sin^2\theta$  term in the numerator.

## APPENDIX B: BCS-GAP EQUATIONS

We treat Eq. (20) in the mean-field approximation and obtain the BCS-gap equations for the band-space gaps as

$$-\Delta_h(\mathbf{k}) = [U_s + U_d \cos 2\phi_h(\mathbf{k})] \int_{\mathbf{p}} \frac{\tanh \frac{E_X(\mathbf{p})}{2T}}{2E_X(\mathbf{p})} \cos^2 \phi_X(\mathbf{p}) \Delta_X(\mathbf{p}) + [U_s - U_d \cos 2\phi_h(\mathbf{k})] \int_{\mathbf{p}} \frac{\tanh \frac{E_Y(\mathbf{p})}{2T}}{2E_Y(\mathbf{p})} \cos^2 \phi_Y(\mathbf{p}) \Delta_Y(\mathbf{p}), \quad (\text{B1})$$

$$-\Delta_X(\mathbf{k}) = \cos^2 \phi_X(\mathbf{k}) \left[ \int_{\mathbf{p}} \frac{\tanh \frac{E_h(\mathbf{p})}{2T}}{2E_h(\mathbf{p})} [U_s + U_d \cos 2\phi_h(\mathbf{p})] \Delta_h(\mathbf{p}) + J_{ee} \int_{\mathbf{p}} \frac{\tanh \frac{E_Y(\mathbf{p})}{2T}}{2E_Y(\mathbf{p})} \cos^2 \phi_Y(\mathbf{p}) \Delta_Y(\mathbf{p}) \right], \quad (\text{B2})$$

$$-\Delta_Y(\mathbf{k}) = \cos^2 \phi_Y(\mathbf{k}) \left[ \int_{\mathbf{p}} \frac{\tanh \frac{E_h(\mathbf{p})}{2T}}{2E_h(\mathbf{p})} [U_s - U_d \cos 2\phi_h(\mathbf{p})] \Delta_h(\mathbf{p}) + J_{ee} \int_{\mathbf{p}} \frac{\tanh \frac{E_X(\mathbf{p})}{2T}}{2E_X(\mathbf{p})} \cos^2 \phi_X(\mathbf{p}) \Delta_X(\mathbf{p}) \right], \quad (\text{B3})$$

where  $E_i(\mathbf{p}) = [\xi_i^2(\mathbf{p}) + |\Delta_i(\mathbf{p})|^2]^{1/2}$  is the typical Bogoliubov quasiparticle spectrum, and momentum integration is confined to an energy interval  $[-\Lambda, \Lambda]$  around the Fermi surface. Near  $T_c$  the linearized gap equations are

$$\Delta_1 + \Delta_2 \cos 2\phi_h = -\ln \frac{\Lambda}{T_c} [N_X \Delta_3 (U_s + U_d \cos 2\phi_h) \langle \cos^4 \phi_X \rangle + N_Y \Delta_4 (U_s - U_d \cos 2\phi_h) \langle \cos^4 \phi_Y \rangle], \quad (\text{B4})$$

$$\Delta_3 = -\ln \frac{\Lambda}{T_c} [N_h \langle (U_s + U_d \cos 2\phi_h) (\Delta_1 + \Delta_2 \cos 2\phi_h) \rangle + N_Y \Delta_4 J_{ee} \langle \cos^4 \phi_Y \rangle], \quad (\text{B5})$$

$$\Delta_4 = -\ln \frac{\Lambda}{T_c} [N_h \langle (U_s - U_d \cos 2\phi_h) (\Delta_1 + \Delta_2 \cos 2\phi_h) \rangle + N_X \Delta_3 J_{ee} \langle \cos^4 \phi_X \rangle]. \quad (\text{B6})$$

### APPENDIX C: DEPENDENCE OF $\frac{\Delta_2}{\Delta_1}$ ON THE NEMATIC ORDER

We set  $J_{ee} = 0$  in this Appendix, and we compute the ratio  $\frac{\Delta_2}{\Delta_1}$  analytically. The largest eigenvalue  $\lambda$  of the matrix equation (24) corresponding to the leading superconducting instability turns out to be

$$\lambda = \left[ \frac{N_h}{2} \left[ g_0 + 2\alpha \langle \cos 2\phi_h \rangle g_1 + \alpha^2 \langle \cos^2 2\phi_h \rangle g_0 \right. \right. \\ \left. \left. + \sqrt{4\alpha^2 (\langle \cos 2\phi_h \rangle^2 - \langle \cos^2 2\phi_h \rangle) (g_0^2 - g_1^2) + (g_0 + 2\alpha \langle \cos 2\phi_h \rangle g_1 + \alpha^2 \langle \cos^2 2\phi_h \rangle g_0)^2} \right] \right]^{1/2}, \quad (\text{C1})$$

where

$$g_0 = N_X \langle \cos^4 \phi_X \rangle + N_Y \langle \cos^4 \phi_Y \rangle \quad (\text{C2})$$

and

$$g_1 = N_X \langle \cos^4 \phi_X \rangle - N_Y \langle \cos^4 \phi_Y \rangle. \quad (\text{C3})$$

In the tetragonal phase,  $g_1 = 0$  and  $g_0 = 2N_X \langle \cos^4 \phi_X \rangle$  (for our band parameters,  $g_0 \approx 0.1$ ). With increasing electron nematic order  $\Phi_e$ ,  $\langle \cos^4 \phi_Y \rangle$  decreases since the  $Y$  pocket becomes mostly of  $d_{xy}$  nature. As a result,  $g_0 - g_1$  decreases with  $\Phi_e$ .

To calculate the ratio  $\frac{\Delta_2}{\Delta_1}$ , we rewrite Eq. (B4),

$$\Delta_2 = -\frac{\alpha}{\lambda} [N_X \Delta_3 \langle \cos^4 \phi_X \rangle - N_Y \Delta_4 \langle \cos^4 \phi_Y \rangle], \quad (\text{C4})$$

which can be computed from Eqs. (B5) and (B6), and we get the following relation:

$$\Delta_2 = \frac{N_h \alpha}{\lambda^2} [\Delta_1 (g_1 + \alpha \langle \cos 2\phi_h \rangle g_0) + \Delta_2 (g_1 \langle \cos 2\phi_h \rangle + \alpha \langle \cos^2 2\phi_h \rangle g_0)]. \quad (\text{C5})$$

One rearranges Eq. (C5) to find the ratio

$$\frac{\Delta_2}{\Delta_1} = \alpha N_h \frac{g_1 + \alpha \langle \cos 2\phi_h \rangle g_0}{\lambda^2 - \alpha N_h (g_1 \langle \cos 2\phi_h \rangle + \alpha \langle \cos^2 2\phi_h \rangle g_0)} = 2\alpha \frac{g_1 + \alpha \langle \cos 2\phi_h \rangle g_0}{(1 - \alpha^2 \langle \cos^2 2\phi_h \rangle) + D}, \quad (\text{C6})$$

where

$$D = \sqrt{4\alpha^2 (\langle \cos 2\phi_h \rangle^2 - \langle \cos^2 2\phi_h \rangle) (1 - g_1^2) + (1 + 2\alpha \langle \cos 2\phi_h \rangle g_1 + \alpha^2 \langle \cos^2 2\phi_h \rangle g_0)^2} \quad (\text{C7})$$

and

$$g(\Phi_e) = \frac{g_1}{g_0} = \frac{N_X \langle \cos^4 \phi_X \rangle - N_Y \langle \cos^4 \phi_Y \rangle}{N_X \langle \cos^4 \phi_X \rangle + N_Y \langle \cos^4 \phi_Y \rangle}. \quad (\text{C8})$$

Even though nematic order couples  $s$ - and  $d$ -wave symmetry and brings angular dependence to the superconducting gap function in the primary  $s$ -wave state, one finds that  $\frac{\Delta_2}{\Delta_1} = 0$  when the numerator of Eq. (C6) vanishes,

$$(N_X \langle \cos^4 \phi_X \rangle - N_Y \langle \cos^4 \phi_Y \rangle) + \alpha \langle \cos 2\phi_h \rangle (N_X \langle \cos^4 \phi_X \rangle + N_Y \langle \cos^4 \phi_Y \rangle) = 0. \quad (\text{C9})$$

For this case, the gap function on the hole pocket becomes purely  $s$ -wave, despite the presence of nematic order.

- [1] A. I. Coldea and M. D. Watson, *Annu. Rev. Condens. Matter Phys.* **9**, 125 (2018).
- [2] A. E. Böhmer and A. Kreisel, *J. Phys. Condens. Matter* **30**, 023001 (2017).
- [3] R. M. Fernandes and A. V. Chubukov, *Rep. Prog. Phys.* **80**, 014503 (2016).
- [4] Y. S. Kushnirenko, D. V. Evtushinsky, T. K. Kim, I. Morozov, L. Harnagea, S. Wurmehl, S. Aswartham, B. Büchner, A. V. Chubukov, and S. V. Borisenko, *Phys. Rev. B* **102**, 184502 (2020).
- [5] Y. Cao, D. Rodan-Legrain, J. M. Park, N. F. Q. Yuan, K. Watanabe, T. Taniguchi, R. M. Fernandes, L. Fu, and P. Jarillo-Herrero, *Science* **372**, 264 (2021).
- [6] K. Matano, M. Kriener, K. Segawa, Y. Ando, and G.-q. Zheng, *Nat. Phys.* **12**, 852 (2016).
- [7] S. Yonezawa, K. Tajiri, S. Nakata, Y. Nagai, Z. Wang, K. Segawa, Y. Ando, and Y. Maeno, *Nat. Phys.* **13**, 123 (2017).
- [8] Y. Pan, A. M. Nikitin, G. K. Araizi, Y. K. Huang, Y. Matsushita, T. Naka, and A. de Visser, *Sci. Rep.* **6**, 28632 (2016).
- [9] T. Asaba, B. J. Lawson, C. Tinsman, L. Chen, P. Corbae, G. Li, Y. Qiu, Y. S. Hor, L. Fu, and L. Li, *Phys. Rev. X* **7**, 011009 (2017).
- [10] R. M. Fernandes and O. Vafek, *Phys. Rev. B* **90**, 214514 (2014).
- [11] L. C. Rhodes, J. Böker, M. A. Müller, M. Eschrig, and I. M. Eremin, *npj Quantum Mater.* **6**, 45 (2021).
- [12] M. D. Watson, T. K. Kim, A. A. Haghighirad, N. R. Davies, A. McCollam, A. Narayanan, S. F. Blake, Y. L. Chen, S. Ghannadzadeh, A. J. Schofield, M. Hoesch, C. Meingast, T. Wolf, and A. I. Coldea, *Phys. Rev. B* **91**, 155106 (2015).
- [13] A. V. Chubukov, M. Khodas, and R. M. Fernandes, *Phys. Rev. X* **6**, 041045 (2016).
- [14] S. Onari, Y. Yamakawa, and H. Kontani, *Phys. Rev. Lett.* **116**, 227001 (2016).
- [15] L. Fanfarillo, J. Mansart, P. Toulemonde, H. Cercellier, P. Le Fevre, F. Bertran, B. Valenzuela, L. Benfatto, and V. Brouet, *Phys. Rev. B* **94**, 155138 (2016).
- [16] L. Benfatto, B. Valenzuela, and L. Fanfarillo, *npj Quantum Mater.* **3**, 1 (2018).
- [17] M. Udina, M. Grilli, L. Benfatto, and A. V. Chubukov, *Phys. Rev. Lett.* **124**, 197602 (2020).
- [18] X. Wu, Y. Liang, H. Fan, and J. Hu, [arXiv:1603.02055](https://arxiv.org/abs/1603.02055) v1.
- [19] R.-Q. Xing, L. Classen, M. Khodas, and A. V. Chubukov, *Phys. Rev. B* **95**, 085108 (2017); L. Classen, R.-Q. Xing, M. Khodas, and A. V. Chubukov, *Phys. Rev. Lett.* **118**, 037001 (2017); S. Baek, D. Efremov, J. M. Ok, J. S. Kim, J. van den Brink, and B. Büchner, *Nat. Mater.* **14**, 210 (2014); R.-Q. Xing, L. Classen, and A. V. Chubukov, *Phys. Rev. B* **98**, 041108(R) (2018).
- [20] M. D. Watson, A. A. Haghighirad, L. C. Rhodes, M. Hoesch, and T. K. Kim, *New J. Phys.* **19**, 103021 (2017).
- [21] M. Yi, H. Pfau, Y. Zhang, Y. He, H. Wu, T. Chen, Z. R. Ye, M. Hashimoto, R. Yu, Q. Si, D.-H. Lee, P. Dai, Z.-X. Shen, D. H. Lu, and R. J. Birgeneau, *Phys. Rev. X* **9**, 041049 (2019).
- [22] S. S. Huh, J. J. Seo, B. S. Kim, S. H. Cho, J. K. Jung, S. Kim, Y. Y. Koh, C. I. Kwon, J. S. Kim, W. S. Kyung, J. D. Denlinger, Y. H. Kim, B. N. Chae, N. D. Kim, Y. K. Kim, and C. Kim, *Commun. Phys.* **3**, 52 (2020).
- [23] C. Cai, T. T. Han, Z. G. Wang, L. Chen, Y. D. Wang, Z. M. Xin, M. W. Ma, Y. Li, and Y. Zhang, *Phys. Rev. B* **101**, 180501(R) (2020).
- [24] C. Cai, T. T. Han, Z. G. Wang, L. Chen, Y. D. Wang, Z. M. Xin, M. W. Ma, Y. Li, and Y. Zhang, *Chin. Phys. B* **29**, 077401 (2020).
- [25] L. C. Rhodes, M. D. Watson, A. A. Haghighirad, D. V. Evtushinsky, and T. K. Kim, *Phys. Rev. B* **101**, 235128 (2020).
- [26] D. Steffensen, A. Kreisel, P. J. Hirschfeld, and B. M. Andersen, *Phys. Rev. B* **103**, 054505 (2021).
- [27] N. Lanata, H. U. R. Strand, G. Giovannetti, B. Hellsing, L. de' Medici, and M. Capone, *Phys. Rev. B* **87**, 045122 (2013).
- [28] L. de' Medici, *Weak and Strong Correlations in Fe Superconductors*, Springer Series in Materials Science Vol. 211 (Springer, Cham, Heidelberg, New York, Dordrecht, London, 2015).
- [29] A. Chubukov, *Annu. Rev. Condens. Matter Phys.* **3**, 57 (2012).
- [30] P. Hirschfeld, *C. R. Phys.* **17**, 197 (2016).
- [31] J. K. Glasbrenner, I. I. Mazin, H. O. Jeschke, P. J. Hirschfeld, R. M. Fernandes, and R. Valenti, *Nat. Phys.* **11**, 953 (2015).
- [32] E. Bascones, B. Valenzuela, and M. J. Calderón, *C. R. Phys.* **17**, 36 (2016).
- [33] S. Graser, T. Maier, P. Hirschfeld, and D. Scalapino, *New J. Phys.* **11**, 025016 (2009).
- [34] J. Kang, R. M. Fernandes, and A. Chubukov, *Phys. Rev. Lett.* **120**, 267001 (2018).
- [35] J. Kang, A. V. Chubukov, and R. M. Fernandes, *Phys. Rev. B* **98**, 064508 (2018).
- [36] P. Sprau, A. Kostin, A. Kreisel, A. E. Böhmer, T. V., P. C. Canfield, S. Mukherjee, P. J. Hirschfeld, B. M. Andersen, and J. C. S. Davis, *Science* **357**, 75 (2017); A. Kreisel, B. M. Andersen, P. O. Sprau, A. Kostin, J. C. Seamus Davis, and P. J. Hirschfeld, *Phys. Rev. B* **95**, 174504 (2017).
- [37] A. Fedorov, A. Yaresko, T. K. Kim, Y. Kushnirenko, E. Haubold, T. Wolf, M. Hoesch, A. Gruneis, B. Buechner, and S. V. Borisenko, *Sci. Rep.* **6**, 36834 (2017).
- [38] D. V. Chichinadze and A. V. Chubukov, *Phys. Rev. B* **99**, 024509 (2019).
- [39] G.-Y. Chen, X. Zhu, H. Yang, and H.-H. Wen, *Phys. Rev. B* **96**, 064524 (2017).
- [40] Y. Sun, S. Kittaka, S. Nakamura, T. Sakakibara, K. Irie, T. Nomoto, K. Machida, J. Chen, and T. Tamegai, *Phys. Rev. B* **96**, 220505(R) (2017).
- [41] Y. Sun, S. Kittaka, S. Nakamura, T. Sakakibara, P. Zhang, S. Shin, K. Irie, T. Nomoto, K. Machida, J. Chen, and T. Tamegai, *Phys. Rev. B* **98**, 064505 (2018).
- [42] L. Jiao, C.-L. Huang, S. Rößler, C. Koz, U. K. Rößler, U. Schwarz, and S. Wirth, *Sci. Rep.* **7**, 44024 (2017).
- [43] H. Cercellier, P. Rodière, P. Toulemonde, C. Marcenat, and T. Klein, *Phys. Rev. B* **100**, 104516 (2019).
- [44] T. Klein *et al.* (private communication).
- [45] V. Cvetkovic and O. Vafek, *Phys. Rev. B* **88**, 134510 (2013).
- [46] M. H. Christensen, R. M. Fernandes, and A. V. Chubukov, *Phys. Rev. Research* **2**, 013015 (2020).
- [47] J.-Y. Lin, Y. S. Hsieh, D. A. Chareev, A. N. Vasiliev, Y. Parsons, and H. D. Yang, *Phys. Rev. B* **84**, 220507(R) (2011).
- [48] F. Hardy, M. He, L. Wang, T. Wolf, P. Schweiss, M. Merz, M. Barth, P. Adelman, R. Eder, A.-A. Haghighirad, and C. Meingast, *Phys. Rev. B* **99**, 035157 (2019).
- [49] Y. Mizukami, M. Haze, O. Tanaka, K. Matsuura, D. Sano, J. Böker, I. Eremin, S. Kasahara, Y. Matsuda, and T. Shibauchi, [arXiv:2105.00739](https://arxiv.org/abs/2105.00739).

- [50] S. Karlsson, P. Strobel, A. Sulpice, C. Marcenat, M. Legendre, F. Gay, S. Pairis, O. Leynaud, and P. Toulemonde, *Supercond. Sci. Technol.* **28**, 105009 (2015).
- [51] S. Rößler, C.-L. Huang, L. Jiao, C. Koz, U. Schwarz, and S. Wirth, *Phys. Rev. B* **97**, 094503 (2018).
- [52] F. Marsiglio and J. P. Carbotte, *Phys. Rev. B* **33**, 6141 (1986).
- [53] J. P. Carbotte, *Rev. Mod. Phys.* **62**, 1027 (1990).
- [54] T. M. Mishonov, S. I. Klenov, and E. S. Penev, *Phys. Rev. B* **71**, 024520 (2005).
- [55] T. M. Mishonov, V. L. Pokrovsky, and H. Wei, *Phys. Rev. B* **71**, 012514 (2005).
- [56] E. J. Nicol and J. P. Carbotte, *Phys. Rev. B* **71**, 054501 (2005).
- [57] M. Zehetmayer, H. W. Weber, and E. Schachinger, *J. Low Temp. Phys.* **133**, 407 (2003).
- [58] M. Zehetmayer, *Supercond. Sci. Technol.* **26**, 043001 (2013).
- [59] S. Maiti and A. V. Chubukov, *Phys. Rev. B* **82**, 214515 (2010).